Applied Catalysis B: Environment and Energy 384 (2026) 126214

Contents lists available at ScienceDirect

Applied Catalysis B: Environment and Energy

journal homepage: www.elsevier.com/locate/apcatb

Microwave-assisted catalytic upcycling of polyolefin wastes into hydrogen and carbon nanotubes over Pt-promoted Fe/Ni bimetallic catalysts

Yuhao Qiao [a], Xuanyan Chen [a], Zixuan Wang [a], Weihao Xu [a], Zecheng Gan [a], Jun Wang [a,b,*]

[a] Advanced Materials Thrust, The Hong Kong University of Science and Technology (Guangzhou), Guangzhou 511400, China
[b] Department of Chemical and Biological Engineering, The Hong Kong University of Science and Technology, Clear Water Bay, 999077, Hong Kong, China

ARTICLE INFO

Keywords:
Microwave
Fe/Ni-Pt catalysts
Plastic upcycling
Hydrogen
Carbon nanotubes
Oxygen vacancies
Acid sites

ABSTRACT

The rapid accumulation of plastic waste poses a critical environmental challenge and demands effective upcycling strategies to advance a circular economy. Microwave-assisted catalysis offers a low-energy, highly efficient alternative to conventional thermal processes; however, the principles guiding catalyst design and the underlying reaction mechanisms in this context remain insufficiently understood. Here, we report a microwave-assisted catalytic approach for converting polyolefin waste into high-value hydrogen (H_2) and multi-walled carbon nanotubes (MWCNTs) using a Pt-promoted Fe/Ni bimetallic catalyst. The catalyst design leverages incorporation of a very small amount of Pt (e.g., 0.3 %) to substantially lower the oxygen vacancy formation energy, as revealed by experimental characterization and density functional theory (DFT) calculations, resulting in a 3.3-fold increase in strong acid site density. These modifications reduce the activation barriers for C–H and C–C bond cleavage, enabling efficient polyolefin conversion. Butane was employed as a model compound in DFT calculation to elucidate the polyethylene decomposition reaction mechanism, which proceeds via terminal C–H bond activation, formation of conjugated olefins, and subsequent deep dehydrogenation. Under microwave treatment, the Fe/Ni–0.3 %Pt catalyst achieved an H_2 yield of 53.9 mmol/g and a selectivity of 90 % from low-density polyethylene (LDPE). The carbonaceous co-products were mainly high-quality MWCNTs exhibiting excellent electromagnetic interference (EMI) shielding performance. This integrated catalytic–microwave approach demonstrates a scalable route for transforming various polyolefin wastes into clean H_2 and advanced carbon materials, offering a viable pathway for sustainable energy and material production within a circular economy framework.

1. Introduction

To date, over 8 billion metric tons of virgin plastics have been produced globally, with approximately 80 % ending up as waste in landfills and natural environments, which poses significant environmental concerns [1,2]. Polyolefins, including polyethylene (PE) and polypropylene (PP), account for more than 50 % of global plastic production [3]. However, their recycling remains a significant challenge due to their highly inert nature, as they are composed primarily of strong C–C and C–H bonds [4]. Nonetheless, given their elemental composition, polyolefin waste represents a valuable feedstock for the production of hydrogen and functional carbon materials, offering a promising strategy to mitigate plastic pollution while simultaneously addressing the growing demand for sustainable energy resources [5,6]. In a typical pyrolysis process, long-chain polyolefins such as PE undergo random homolytic cleavage of C–C bonds, producing smaller hydrocarbon fragments including alkanes and alkenes [7]. These volatile fragments adsorb onto the catalyst surface, where metal sites catalyze subsequent dehydrogenation and hydrogenolysis reactions, generating surface alkyl intermediates [8,9]. Simultaneously, acid sites on the catalyst promote scission reactions, further cracking larger intermediates into light hydrocarbons, carbonaceous materials, and H_2 [10].

Microwave-assisted catalytic processes have garnered increasing attention for their ability to effectively convert plastic waste into high-value products [4,11,12]. This technology utilizes microwave radiation for selective heating of the reaction system, enhancing energy efficiency and reaction selectivity [4,13]. The interaction between microwaves and catalysts facilitates faster and more uniform heating, reducing the need for high temperatures and expanding the range of feasible catalytic transformations. Moreover, microwave irradiation

* Corresponding author at: Advanced Materials Thrust, The Hong Kong University of Science and Technology (Guangzhou), Guangzhou 511400, China.
E-mail address: junwangc@hkust-gz.edu.cn (J. Wang).

https://doi.org/10.1016/j.apcatb.2025.126214
Received 15 August 2025; Received in revised form 15 October 2025; Accepted 16 November 2025
Available online 19 November 2025

may induce non-thermal effects that lower activation energy and alter reaction pathways, enhancing selectivity by favoring specific bond cleavages during the catalytic cracking of liquid hydrocarbons and polyolefin wastes [14]. In this context, Hu and co-workers showed that microwave irradiation generates localized "hot-metal" domains on microwave-absorbing catalysts, producing intense thermal and electric field gradients for the activation of C–H and C–C bonds [15,16]. Combined experimental and modeling studies on methane dehydroaromatization (DHA) further demonstrated that the synergistic thermal and non-thermal effects of microwaves not only enhance conversion and aromatic yields but also alter coke formation dynamics and improve catalyst stability through field-induced polarization [15,17,18]. Notably, thermal catalytic decomposition of plastics yields moderate hydrogen production, typically ranging from 20 to 40 mmol H_2 per gram of plastic. However, microwave-initiated catalytic decomposition demonstrated a more efficient pathway, achieving hydrogen yields exceeding 40 mmol/g [11,14].

As transition metals with partially filled 3d orbitals, Fe, Ni, and Co exhibit high catalytic activity by facilitating the dissociation of hydrocarbon molecules through electron acceptance, thereby promoting the formation of lighter products [19,20]. In addition, these metals possess high carbon solubility, enabling them to serve as nucleation centers for graphitic carbon deposition and the growth of carbon nanotubes (CNTs) [21]. The combination of strong catalytic performance, efficient energy conversion under microwave irradiation, and ability to generate valuable carbon nanostructures makes them ideal candidates for plastic upcycling applications [22,23]. However, Fe, Co, and Ni alone do not yield optimal catalytic performance. Fe-based catalysts are widely regarded as cost-effective and catalytically efficient for the conversion of plastic waste into hydrogen and carbon materials, owing to their strong C–H bond activation ability and excellent microwave-induced heating properties [24]. However, iron readily reacts with carbon to form iron carbide (Fe_3C), and iron oxides are prone to structural collapse at elevated temperatures, both of which diminish catalytic performance. Some studies reported that Ni-based catalysts exhibited lower hydrogenation activity and H_2 production yield [19,25]. However, some inconsistencies exist in the literature, with certain studies reporting that Ni exhibits better performance than Fe [26]. These discrepancies may arise from variations in experimental conditions such as reaction atmosphere, temperature, and feed composition.

Bimetallic catalysts can overcome these limitations by complementing each other's strengths. The synergistic effects between metal components, as well as the electronic and geometric modifications introduced by secondary metals, lead to enhanced activity, stability, and selectivity [27]. For instance, Li et al. [14] developed a Fe-Al-based catalyst that, when doped with cobalt in a microwave field, efficiently converted into a high-performance Fe/Co alloy. The introduction of cobalt effectively suppressed Fe carburization, enhanced dehydrogenation of plastic feedstocks, and thus increased the overall yield of both hydrogen and carbonaceous products. However, the degree of graphitization of carbon materials was reduced. Zhang et al. [28] proposed an iron-cobalt bimetallic catalyst capable of harvesting nearly 80 % hydrogen while producing abundant carbon nanotubes. Moreover, Fe- and Ni-based catalysts have shown promise in selectively converting plastics into hydrogen and carbon materials, making them ideal candidates for sustainable plastic waste upcycling and recycling [29,30]. Luo et al. [20] investigated Fe/Ni bimetallic catalysts supported on porous silicon carbide (SiC). The combination of a porous structure, enhanced dielectric properties, and catalyst–support interactions facilitated the efficient conversion of plastic waste into high-value products. A synergistic effect between the two metals was observed, with Ni preferentially cleaving =C–H bonds to promote the formation of saturated alkanes, whereas Fe was more effective in breaking C–C and C–H bonds, thereby contributing to the generation of gaseous products. Furthermore, increasing the Fe content led to carbon nanotubes (CNTs) with a higher degree of graphitization. This was attributed to the higher carbon solubility in Fe, which enhanced carbon atom diffusion and deposition, thereby improving the CNT growth process. On the other hand, introduction of Fe into Ni was found to prolong the catalyst's operational lifetime and enhanced the production yield of carbon nanotubes [31]. Other studies also demonstrated that Fe/Ni bimetallic catalysts enable high yields of hydrogen and carbon materials during polypropylene pyrolysis, attributed to their enhanced reducibility and synergistic effects [26]. These effects likely arise from modified electronic structures that facilitate C–H bond dissociation and promote hydrogen spillover, thereby improving catalytic activity and reaction selectivity [32].

Despite significant progress in the development of these bimetallic catalysts, several challenges remain unresolved. Specifically, Fe/Ni bimetallic systems, though promising, suffer from instability at high temperatures, unstable carbide formation, and suboptimal hydrogen selectivity. In this context, noble metals have been incorporated as promoters to enhance catalyst activity and stability in methane decomposition [33–35]. Takenaka et al. investigated methane decomposition over Ni/SiO_2 catalysts promoted with Cu, Rh, Pd, Ir, and Pt [36]. Among these, Pd was found to suppress catalyst deactivation and, through the formation of Pd–Ni bimetallic alloys, improve the yield and the morphology of the resulting carbon nanofibers. In another study, the incorporation of Pt as a promoter in Ni/CeO_2 catalysts enhanced methane decomposition by improving hydrogen yield and catalyst stability, which was attributed to the synergistic interaction between Ni and Pt, their fine dispersion, and proper metal–support interactions [35]. Pt was also found to facilitate hydrogen spillover, accelerating reaction kinetics [37]. However, to the best of our knowledge, the use of noble metals to promote microwave-assisted catalytic decomposition of waste plastics in conjunction with transition metals has not yet been explored. In addition, it is well established that the formation of oxygen vacancies in metal oxides typically arises from the consumption of lattice oxygen under high-temperature and reducing atmospheres [38]. These oxygen vacancies, along with surface acid sites, metal dispersion, and the spatial distribution of active phases, play a critical role in determining the catalytic activity and product selectivity during the thermal decomposition of polymers.

In this study, low-density polyethylene (LDPE) is employed as a model polyolefin to investigate an efficient microwave-assisted catalytic upcycling approach using a Pt-modified Fe/Ni bimetallic catalyst (Fe/Ni–Pt). Fe and Ni act as bifunctional components, offering both strong microwave absorption and catalytic activity, while a very small amount of platinum (e.g. 0.3 % by weight) serves as a promoter to enhance hydrogen dissociation under microwave irradiation. This strategy significantly improves hydrogen yield and selectivity and promotes the formation of high-value carbon nanotubes. A combined experimental and theoretical investigation reveals that Pt incorporation enhances catalytic performance by increasing oxygen vacancy concentration, generating stronger acid sites. These synergistic effects collectively accelerate C–H and C–C bond activation, resulting in higher hydrogen yields and more controlled carbon nanostructure formation. The strategy was successfully extended to other post-consumer polyolefin wastes, demonstrating broad applicability and high efficiency. Moreover, the resulting solid products exhibit excellent electromagnetic interference (EMI) shielding properties for functional applications. Overall, this work presents a promising pathway for sustainable plastic waste valorization into clean energy and functional materials.

2. Experimental section

2.1. Chemicals and materials

Methanol, iron nitrate nonahydrate ($Fe(NO_3)_3{\cdot}9H_2O$), nickel nitrate hexahydrate ($Ni(NO_3)_2{\cdot}6H_2O$), citric acid, and chloroplatinic acid were purchased from Macklin Reagent Co., Ltd. (Shanghai, China). Low-density polyethylene (LDPE) FE 8004 was obtained from Qatar Petrochemical Company. All materials were used as received without further

purification. The real-world plastic waste of rinse bottle (low density polyethylene), milk containers (high-density polyethylene), plastic wrap (linear low-density polyethylene) and storage box (polypropylene) used in this study were collected from waste materials used by large supermarket chains and the laboratory.

2.2. Preparation of catalyst

The catalyst was synthesized using a combustion method. Fe $(NO_3)_3 \cdot 9H_2O$ and $Ni(NO_3)_2 \cdot 6H_2O$ were mixed in a molar ratio of 1:2, followed by the addition of citric acid. Distilled water was then added, and the mixture was stirred until all solids were completely dissolved. Methanol and a chloroplatinic acid solution were subsequently introduced, and the solution was ultrasonicated for 15 min, followed by an additional 5 min of stirring. The resulting solution was exposed to a UV xenon lamp for 30 min. After UV exposure, the solution was placed in a vacuum oven for an appropriate period of time to form a viscous gel. This gel was calcined at 350 °C in a nitrogen atmosphere for 3.5 h, after which it was collected and ground into a fine powder.

2.3. Microwave catalytic upcycling of LDPE

LDPE was ground into a fine powder using a ball mill under cryogenic conditions and then physically mixed with the catalyst particles to ensure even dispersion. The mixture was then transferred to a reaction tube, which was placed in the reaction chamber of a microwave reactor (MKP-WT1HA, Qingdao Microwave Applied Technology Co. Ltd). The reactor operated at a fixed frequency of 2450 MHz, with an adjustable output power ranging from 10 % to 100 % of its maximum capacity of 2000 W. LDPE was mixed with the catalyst at a 1:1 mass ratio and subjected to microwave treatment at the designated temperature and power for 5 min, unless otherwise specified. Nitrogen gas was introduced into the system at a flow rate of 10 mL/min for 5 min to purge air from the reaction tube prior to microwave radiation. In the catalyst recycling experiments, the spent catalyst was dispersed in ethanol and subjected to ultrasonication for 30 min, followed by a 15 min resting period to separate carbonaceous materials from the catalyst. The recovered catalyst was reused directly in subsequent reaction cycles by adding fresh LDPE powder, without the addition of new catalyst.

2.4. Characterization

Gaseous products were analyzed using gas chromatography (GC, ISQ 7610, Thermo Fisher Scientific Inc.), while a mass spectrometer (MS, ISQ1600, Thermo Fisher Scientific Inc.) was employed to identify intermediate reaction species. Hydrogen selectivity was defined as the volume fraction of H_2 gas to the total gaseous products, as determined by GC (Eq. 1). It reflects the purity of H_2 in the gaseous products. Hydrogen yield was calculated as the number of moles of hydrogen produced per gram of plastic feedstock (Eq. 2). Hydrogen efficiency was determined using Eq. 3, and it represents the ratio of hydrogen atoms in the generated H_2 gas to the theoretical number of hydrogen atoms originally present in the plastic (Eq. 3). The overall microwave-assisted plastic upcycling process is illustrated schematically in Fig. 1.

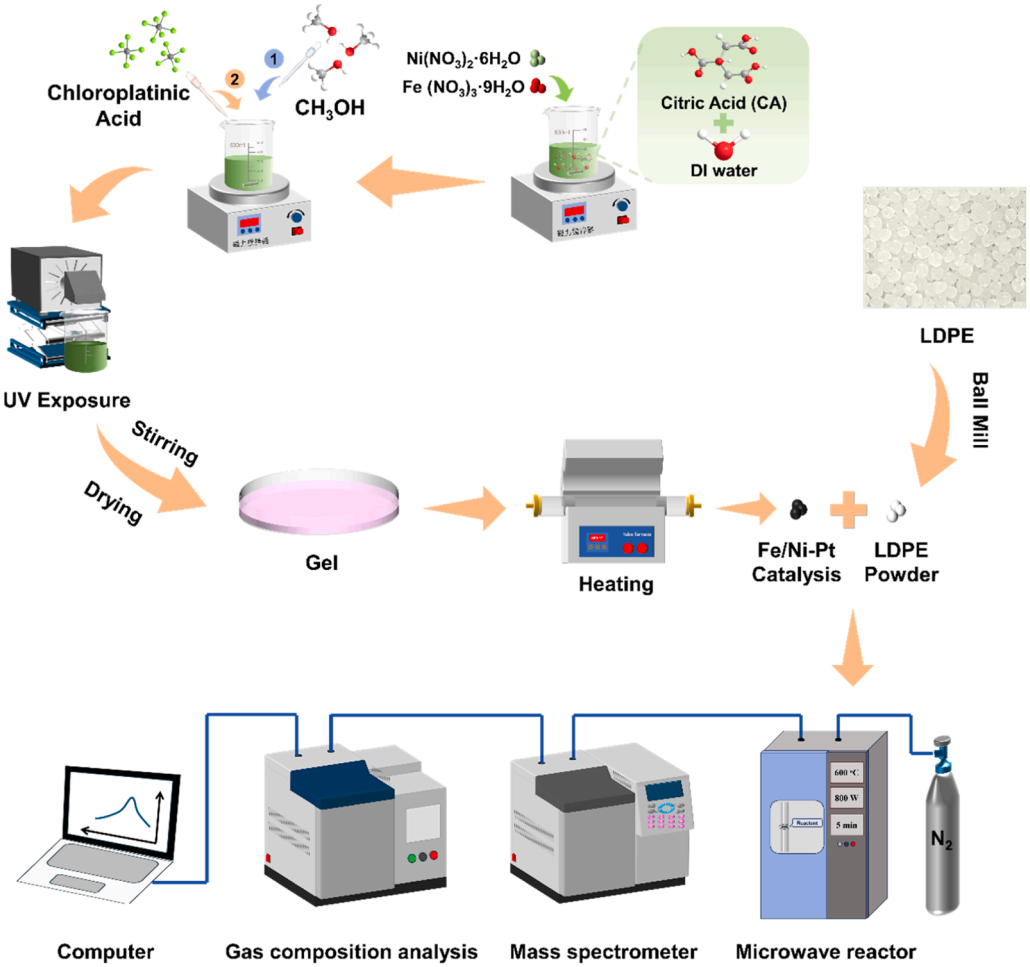

Fig. 1. Schematic for catalyst preparation, microwave-assisted PE upcycling, and product analysis.

$$Hydrogen\ selectivity = \frac{Volume\ of\ H_2}{Total\ volume\ of\ all\ the\ gases}\ (\%) \quad (1)$$

$$H_2\ yield = \frac{Mole\ of\ H_2\ produced}{Mass\ of\ plastic}(mmol g_{plastic}^{-1}) \quad (2)$$

$$Hydrogen\ efficiency = \frac{Total\ mass\ of\ H\ contained\ in\ H_2(g)}{Theoretical\ mass\ of\ H\ in\ plastic(g)}\ (\%) \quad (3)$$

The morphology of the solid products, i.e., the catalysts and carbon materials, was examined using a Hitachi SU5000 high-resolution scanning electron microscope (SEM), a Thermo Fisher Scientific Talos F200X high-resolution transmission electron microscope (HRTEM) and FEI Theims Z High-angle annular dark-field scanning transmission electron microscopy (HAADF-STEM) with aberration correction. Crystallographic analysis was performed using a Malvern PANalytical Empyrean 3.0 multipurpose X-ray diffractometer (XRD) over a 2θ range of 10°–90°. The surface elemental valence states and oxygen vacancies of the samples were investigated using an X-ray photoelectron spectroscopy (XPS) with a PHI VersaProbe 4 system (ULVAC-PHI). The elemental components of the catalyst were analyzed by Malvern PANalytical Energy Dispersive X-Ray Fluorescence Spectrometer (XRF). The carbon species generated during the microwave reaction were characterized using a Renishaw inVia-Qontor Raman spectrometer. The acidity test was conducted by temperature-programmed desorption (TPD) in an NH_3 atmosphere using BelCata II Catalyst Analyzer.

2.5. Electromagnetic interference (EMI) shielding performance

Owing to their intrinsic dielectric and magnetic properties, the solid materials recovered from the catalytic process, consisting of residual catalyst particles and carbonaceous components, exhibit strong potential for high-value applications in EMI shielding. Samples containing 20, 30, and 40 wt% of the solid material, uniformly dispersed in paraffin wax, were molded into rectangular blocks with dimensions of 22.86 mm × 10.16 mm to meet the X-band waveguide standard. The thickness of the samples was 3 mm. The measurements were conducted using a vector network analyzer (Keysight N5227B, USA). By applying established electromagnetic theory, the scattering parameters (S_{11}, S_{12}, S_{21}, S_{22}) were converted into EMI shielding coefficients, including reflectance (R), transmittance (T), and absorbance (A), using Eqs. (4)-(6). Furthermore, the total shielding effectiveness (SE_T), shielding effectiveness by reflection (SE_R), and shielding effectiveness by absorption (SE_A) were calculated according to Eqs. (7)-(9).

$$R = |S_{11}|^2 = |S_{22}|^2 \quad (4)$$

$$T = |S_{21}|^2 = |S_{12}|^2 \quad (5)$$

$$A = 1 - R - T \quad (6)$$

$$SE_R = 10\log\left(\frac{1}{1-R}\right) \quad (7)$$

$$SE_A = 10\log\left(\frac{1-R}{T}\right) \quad (8)$$

$$SE_T = 10\log\frac{1}{T} \quad (9)$$

2.6. DFT calculations

All first-principles calculations in this work were based on density functional theory using the generalized gradient approximation of Perdew, Burke, and Ernzerhof (GGA-PBE) [39] functional. The projector augmented-wave pseudopotentials[39] were used, as implemented in the Vienna ab initio simulation package (VASP) [40]. The Hubbard-U correction was employed to take the electron-correlation interactions into consideration [41,42]. The effective U values of U_{Hub}(Fe) = 4.0 eV and U_{Hub}(O) = 0.0 eV. A plane-wave energy cutoff of 400 eV and a 1x1x1 Monkhorst-Pack [43] k-point grid were adopted for the supercell of (111) surfaces of Fe_3O_4 with 224 atoms. The configuration contained two layers of Fe atoms and two layers of O atoms, which were separated by 15 Å vacuum. In our investigation, the oxygen vacancy formation energies (E_f) were calculated as [44]:

$$E_f(V_O) = E_{tot}(V_O) - E_{tot}(bulk) - \sum_i n_i\mu_i \quad (10)$$

where $E_{tot}(V_O)$ is the total energy of a (111) surface supercell of either Fe_3O_4 or $Fe_{0.18}Ni_{0.82}O_x$containing an oxygen vacancy; $E_{tot}(bulk)$ is the total energy of the pristine (111) surface with 224 atoms; n_i is the number of atomic species removed from ($n_i < 0$) the supercell to make the oxygen vacancies; μ_i is the chemical potential of atomic species i. The reaction energy barrier (E_{bar}) and reaction energy (ΔE) were obtained by the following formulas:

$$E_{bar} = E_{TS} - E_{IS} \quad (11)$$

$$\Delta E = E_{FS} - E_{IS} \quad (12)$$

where E_{TS}, E_{IS}, and E_{FS} represent the total energy of the transition structure (TS), the initial structure (IS), and the final structure (FS), respectively. In convention, a negative ΔE value represents an exothermic reaction, while a positive ΔE value represents an endothermic reaction. The adsorption energy (E_{ads}) of adsorbate X is calculated according to Eq. 13:

$$E_{ads} = E(gas/slab) - E(gas) - E(slab) \quad (13)$$

where $E(gas/slab)$ is the total energy of the adsorbed system, E(gas) is the single point energy of the butane molecule, and E(slab) is the total energy of the clean surface.

3. Results and discussion

3.1. Structural and compositional analysis of the catalyst

XRD analysis (Fig. 2a) revealed characteristic peaks corresponding to $Fe_{0.18}Ni_{0.82}O_x$ and Fe_3O_4, confirming that these crystalline phases were the primary components of the catalyst. No diffraction peaks related to Pt were detected, likely due to the low loading and high dispersion of Pt in the catalyst [45]. The XRD patterns of Fe/Ni-0.3 %Pt and Fe/Ni-0.15 %Pt closely resembled that of unmodified Fe/Ni catalyst, although variations in peak intensity and broadening were observed. These differences indicate that the introduction of Pt may influence the crystallite size and overall crystallinity of the material.

As shown in Fig. 2b and c, XPS was performed to investigate the surface composition and oxidation states of the catalyst components. For the Fe 2p orbital, two prominent peaks were observed at 710.1 eV and 712.3 eV, corresponding to Fe^{2+} $2p_{3/2}$ and Fe^{3+} $2p_{3/2}$, respectively. Additional peaks at 723.0 eV and 725.4 eV were assigned to Fe^{2+} $2p_{1/2}$ and Fe^{3+} $2p_{1/2}$ [46]. These binding energies are characteristic of iron in both the divalent (Fe^{2+}) and trivalent (Fe^{3+}) oxidation states, which are frequently encountered in iron-based catalysts. The mixed-valent state of iron indicates its intrinsic redox activity, which plays a vital role in promoting reactions requiring electron transfer [47]. In particular, Fe^{2+} acts as an electron donor, while Fe^{3+} serves as an electron acceptor, facilitating the cleavage of chemical bonds in plastics and enhancing overall catalytic efficiency.

In the Ni 2p region, the XPS spectrum displayed peaks at 853.2 eV, 854.5 eV, and 855.8 eV, which were attributed to Ni^0 $2p_{3/2}$, Ni^{2+} $2p_{3/2}$, and Ni^{3+} $2p_{3/2}$, respectively. Additional peaks at 871.5 eV and 876.8 eV were associated with Ni^{2+} $2p_{1/2}$. The presence of Ni^0 confirmed the metallic state of nickel, which is commonly involved in hydrogen

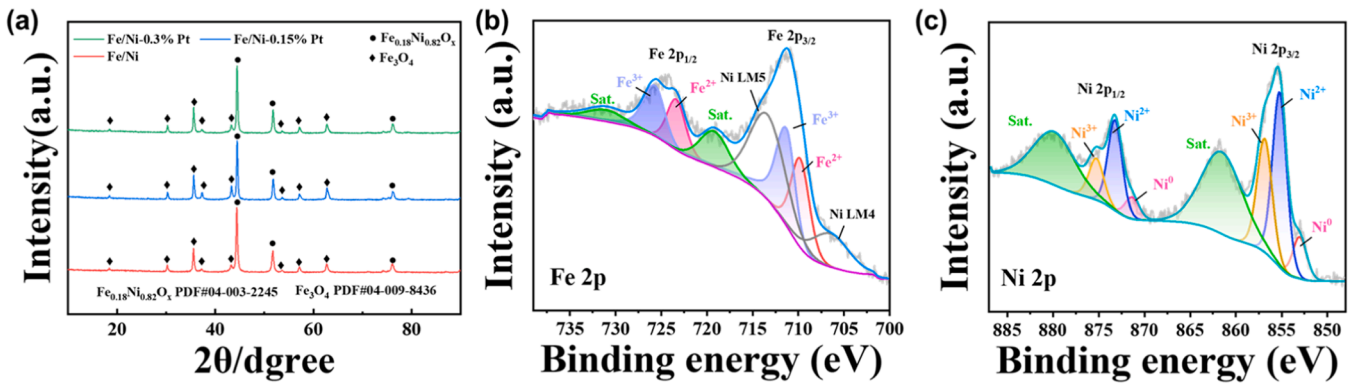

Fig. 2. (a) XRD patterns of the catalysts: Fe/Ni, Fe/Ni-0.15 %Pt, and Fe/Ni-0.3 %Pt. (b) Fe 2p XPS spectra and (c) Ni 2p XPS spectra of the representative Fe/Ni-0.3 %Pt catalyst.

transfer reaction [48–50]. Moreover, previous studies on water splitting have shown that nickel oxide defects can promote the formation of oxygen vacancies, which enhance charge separation and create favorable sites for hydrogen evolution [51] While these findings were observed under photothermal water-splitting conditions, a similar role of oxygen vacancies may contribute to enhanced hydrogen production in microwave-assisted plastic upcycling systems.

The morphology and elemental distribution of the catalysts were characterized using SEM, TEM, HAADF-STEM and EDS. SEM images show that the Pt-modified Fe/Ni catalyst exhibited a rough, porous structure (Fig. 3), which could facilitate microwave adsorption and promote effective plastic-catalyst interactions during conversion [52]. TEM analysis revealed that the metal nanoparticles are partially aggregated into clusters. Moreover, the aberration-corrected, high-resolution HAADF-STEM was employed to directly visualize the Pt species on the Fe/Ni surface. As shown in Fig. 3(g, h), both atomically dispersed Pt and small Pt clusters are observed. The Pt species are relatively uniformly distributed across the catalyst surface, confirming the coexistence of atomic-scale and sub-nanometer Pt domains. Elemental mapping by EDS (Fig. 3b-e) and compositional analysis by XRF (Supplementary data Figure S1) confirm the uniform distribution of Fe, Ni, and Pt throughout the catalyst, with concentrations consistent with the intended synthesis ratios. These results verify the successful incorporation of platinum and validate the structural design of the catalyst.

Because of the very low Pt content (0.3 %) in the optimized catalyst, Pt-related peaks were not detectable in XPS or XRD. A reference sample with a higher Pt loading (10 %) was prepared using the same synthesis protocol and examined by XPS and XRD (Supplementary data Figure S2). XPS analysis of this sample reveals that Pt may exist mainly in the metallic state with a fraction of partially oxidized Pt^{2+}/Pt^{4+} species. XRD analysis further indicates that Pt can form an alloy phase with Fe, identified as $Fe_{0.75}Pt_{0.25}$, while no distinct Pt–Ni alloy peaks were observed. However, more advanced techniques such as synchrotron-based X-ray absorption spectroscopy (XAS) will be needed to confirm the possible oxidation state and alloy formation of Pt in the catalysts with very low Pt loading used in this study.

3.2. Microwave catalytic performance for LDPE deconstruction

Fe/Ni-based catalysts are well recognized for their strong microwave absorption and efficient activation of C–C and C–H bonds, making them highly effective for microwave-assisted catalytic transformations. However, their catalytic performance is strongly influenced by compositional modifications and surface engineering. Zhao et al. [24] reported that iron-nickel bimetallic oxides, such as $Ni_3Fe_1O_x$, possessed outstanding catalytic dehydrogenation activity, achieving a hydrogen yield exceeding 40 mmol/g of plastic. Similarly, Wang et al. [22] developed a Fe/Ni-CeO_2 catalyst supported on carbon nanotubes that produced high-purity hydrogen. The enhanced performance was attributed to the synergistic effect between Fe and Ni, while the CeO_2 phase effectively suppressed coke formation and promoted the reforming of intermediate species. Inspired by these advances, several Fe/Ni-based catalyst formulations were synthesized and compared according to previous studies (Supplementary data Figure S3) [4,11,16,22,24,28]. Among them, the Pt-modified Fe/Ni bimetallic catalyst demonstrated the most promising performance in terms of hydrogen yield and selectivity.

Fig. 4 presents the hydrogen production performance of Fe/Ni-based catalysts in microwave-assisted plastic upcycling. The incorporation of a very small amount of platinum significantly enhanced the hydrogen yield, efficiency, and selectivity compared to the unmodified Fe/Ni catalysts. The Fe/Ni–0.15 %Pt catalyst exhibited significantly improved performance compared to the unmodified Fe/Ni catalyst, and further enhancement was achieved with the Fe/Ni–0.3 %Pt catalyst. This improvement is likely due to the synergistic effect between Pt and the Fe/Ni oxides, which enhanced the supply of reactive oxygen species and weakened the adsorption of by-products (such as CO) on active sites [53]. Additionally, the intrinsic redox activity of Pt may have contributed to more efficient hydrogen evolution under microwave conditions [54,55]. However, when the Pt content was increased from 0.3 % to 0.5 %, the catalytic performance plateaued, with only a marginal increase in hydrogen yield and efficiency (53.9 vs. 54.1 mmol/g and 0.80 vs. 0.81 %). The hydrogen selectivity slightly increased from 0.90 to 0.91. This suggests that beyond a certain threshold, additional platinum does not contribute meaningfully to hydrogen production or selectivity. This may be because excessive Pt occupies the active sites on the surface of the catalyst thereby diminishing the overall catalytic performance [56].

To elucidate the synergistic effect between Pt and the Fe/Ni bimetallic catalyst, control catalysts comprising Fe–Pt and Ni–Pt were synthesized and evaluated. As shown in Fig. 4 and Supplementary data Figure S4, the Ni-Pt catalyst produced a hydrogen yield of only 26.8 mmol/g, while the Fe-Pt catalyst yielded 42.7 mmol/g. Both values were substantially lower than the hydrogen yield achieved by the Fe/Ni-Pt catalyst system, which reached 53.9 mmol/g. These results further highlight the critical role of the Fe/Ni bimetallic framework in achieving superior catalyst performance. The enhanced activity can be attributed to the synergistic interaction between Fe and Ni, which facilitated the formation of abundant and highly active sites. Under microwave irradiation, the catalyst promoted efficient cleavage of C–C and C–H bonds in polymer chains, a key step in hydrogen evolution [26,57]. Fe has a high carbon solubility, and catalysts containing Fe are not prone to deactivation at high temperatures [44]. Additionally, Fe also has the

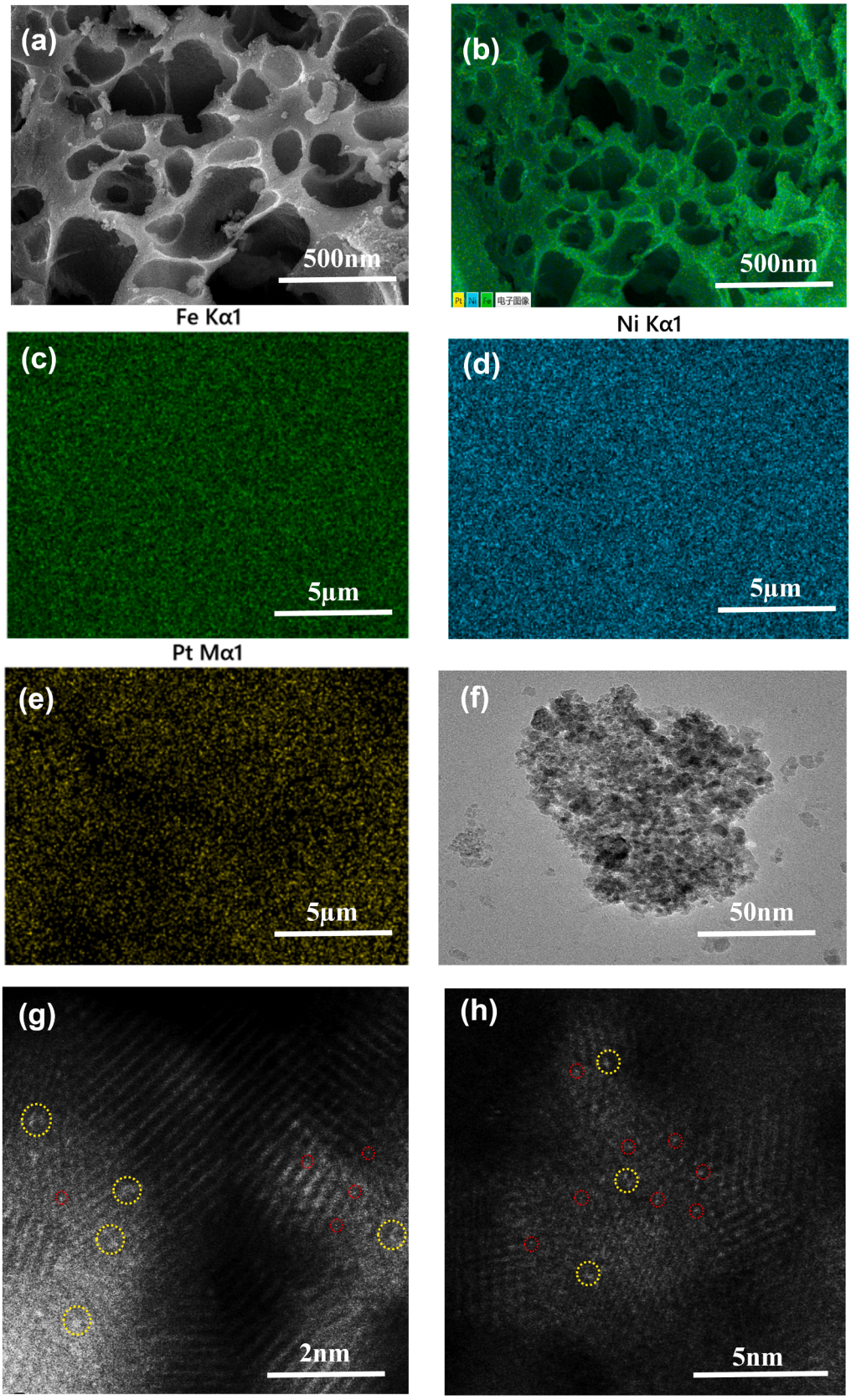

Fig. 3. (a) SEM images of the representative Fe/Ni-0.3 %Pt catalyst. (b–e) EDS elemental mapping images showing the distribution of Fe (green), Ni (blue), and Pt (yellow). (f) TEM images of the Fe/Ni-0.3 %Pt catalyst. (g, h). HAADF-STEM images of the Fe/Ni–Pt catalyst at different magnifications. The yellow circles indicate the aggregated Pt clusters, while the red circles highlight the Pt atoms.

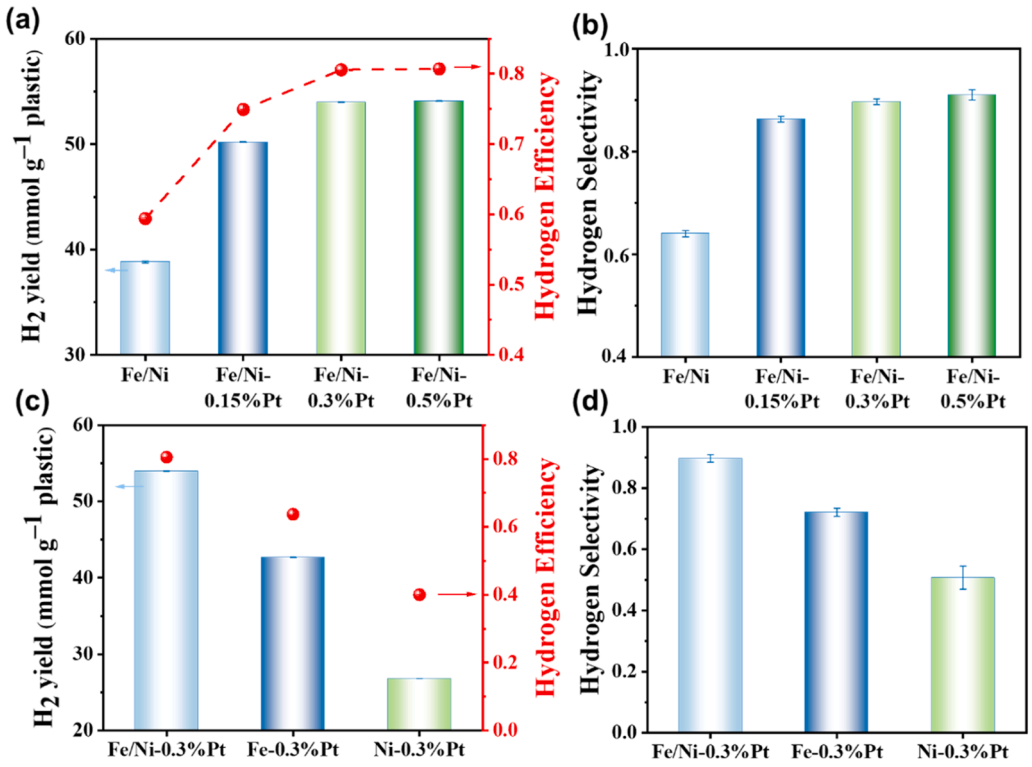

Fig. 4. Hydrogen efficiency, yield and selectivity for various catalysts after microwave treatment at 600 °C for 5 min. (a, b) Fe/Ni bimetallic catalysts modified with different Pt loadings. (c, d) Comparison of monometallic (Fe, Ni) and bimetallic (Fe/Ni) catalysts with Pt modification.

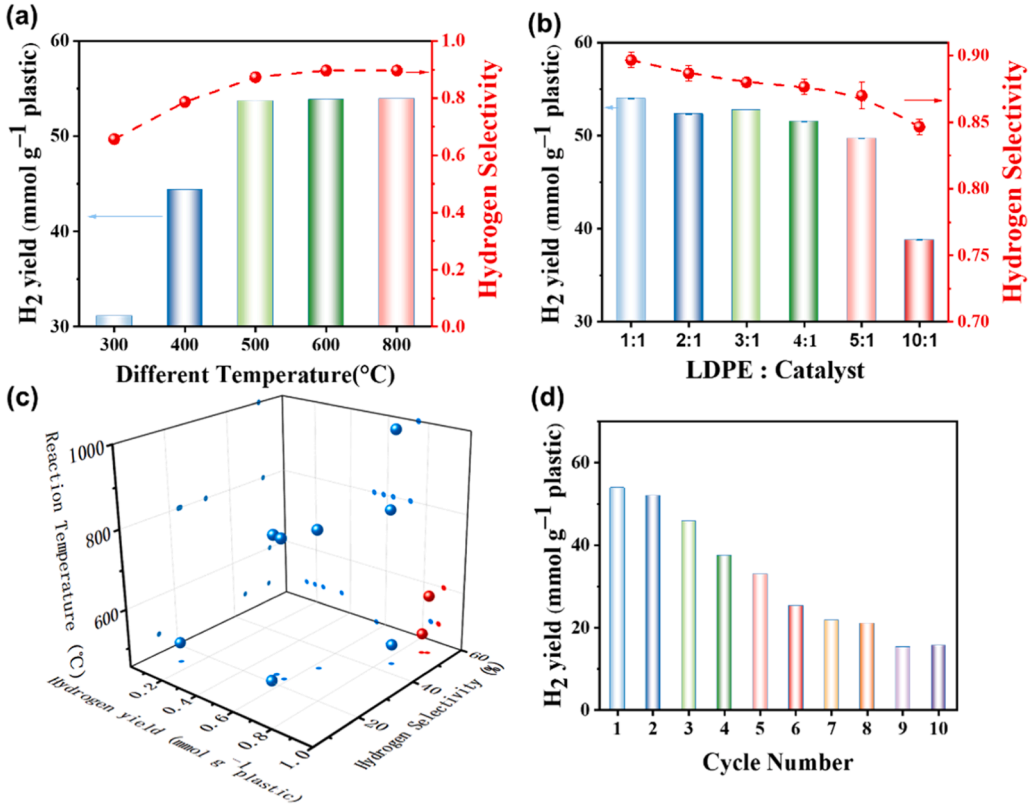

Fig. 5. The hydrogen efficiency, yield and selectivity obtained by the 5-minute microwave treatment of LDPE under different reaction conditions: (a) Fe/Ni-0.3 %Pt catalyst at different temperatures; (b) Fe/Ni-0.3 %Pt catalyst with different feedstock to catalyst ratios; (c) The reaction temperature, hydrogen production rate and selectivity of this work compared with the reference [68] [24] [12] [27] [69] [70] (red represents the results from this work, and blue represents the data from the literature); (d) Cyclic experiments.

partially filled 3d orbitals enabling hydrocarbon activation through electron acceptance, while Ni enhanced hydrogenation–dehydro genation reactions, particularly promoting C–H bond cleavage to generate H_2 [58,59]. The co-existence of Fe and Ni improved the dispersion and accessibility of active metal species. It was argued that bonding can form between Fe and Ni which improved electron transfer capabilities. This improved electron transfer enhanced activation of hydrocarbon intermediates and promoted hydrogen generation pathways [20].

Fig. 5a presents the influence of reaction temperature on H_2 yield and selectivity. As the temperature increased from 300 to 600 °C, both H_2 yield and selectivity improved significantly, reaching 53.9 mmol/g and 90 %, respectively. Further increasing the temperature did not lead to additional improvements in hydrogen production efficiency, suggesting that the catalytic activity reaches a plateau. A similar trend was observed with respect to microwave power, where increased power initially enhanced performance, but beyond a certain threshold, no substantial gains were achieved (Supplementary data Figure S5). Optimal microwave power of 800 W and reaction temperature of 600 °C were identified, under which a maximum hydrogen yield was achieved (Supplementary data Figures S4 and S5). Under these conditions, the Fe/Ni–Pt catalyst exhibited enhanced surface activation driven by strong local electric fields and rapid dielectric heating intrinsic to microwave systems. This accelerated the homolytic cleavage of C–C and C–H bonds in LDPE chains, which were otherwise difficult to break due to the saturated hydrocarbon structure. It was noted that, in thermal pyrolysis of polyethylene for H_2 production, usually a high temperature of 800 °C was needed and only up to ~70 % H_2 were generated [13,60,61], which highlights the superior efficiency of the microwave approach. Previous studies have demonstrated that microwave irradiation significantly enhances thermal distribution by generating localized “hot spots,” which accelerate electron mobility and facilitate their rapid transfer across the surface of metal catalysts, thereby promoting catalytic reactions [62,63]. Moreover, the pronounced mismatch in dielectric constants between the catalyst and PE leads to intense interfacial polarization and dielectric relaxation under the influence of the microwave field. This results in the accumulation of charge carriers at the interface, rapidly activating the reaction [63,64]. In contrast, traditional heating has lower selectivity in providing energy, resulting in a wider heat distribution, more side reactions, and lower catalytic efficiency [11,61].

Fig. 5b shows the influence of the LDPE-to-catalyst mass ratio on catalytic performance. The highest hydrogen yield (54.0 mmol/g plastic) and hydrogen selectivity (90 vol%) were obtained at a 1:1 mass ratio of feedstock to catalyst. As the ratio increased, the hydrogen yields gradually declined, likely due to the excess LDPE with limiting access to active catalytic sites, thereby lowering the overall conversion efficiency. Notably, even at a high LDPE-to-catalyst ratio of 5:1, the hydrogen selectivity remained largely unchanged (~85 %) with a decent H_2 yield of ~50 mmol/g plastic. The results underscore the robustness of the catalyst and its strong intrinsic selectivity toward hydrogen evolution, even under catalyst-limited conditions.

The catalytic LDPE cracking of microwave heating was compared to conventional thermal heating using an electric furnace (Fig. 5a vs. Supplementary data Figure S6). At the same temperature (e.g., 600°C), H_2 yield and selectivity were significantly improved by 26.3 mmol/g and 0.27, respectively, with microwave treatment. In addition, microwave also demonstrated superior energy consumption efficiency, with over 40 % energy saving as compared to traditional thermal pyrolysis (Supplementary data Figure S7), consistent with previous reports [65–67].The enhanced performance under microwave irradiation was attributed to its selective and volumetric heating mechanism. Microwave energy was preferentially absorbed by the bimetallic catalyst, generating rapid and localized thermal hotspots on the catalyst surface. These hotspots created steep temperature gradients that enabled efficient energy transfer to adjacent LDPE chains, promoting the homolytic cleavage of C–H and C–C bonds [11,24]. The strong electric field generated under microwave irradiation can directly polarize alkane molecules, thereby decreasing the electron density of the C–H bonds and facilitating their activation [15]. In contrast, conventional heating relied on bulk thermal conduction, resulting in slower and less uniform heat distribution, which limited the efficiency of catalytic activation.

The recyclability and long-term stability of the catalyst were assessed through 10 consecutive reaction cycles, with ultrasonic treatment applied after each cycle to recover the catalyst from the carbonaceous materials. The catalyst exhibited high stability, maintaining a hydrogen yield of > 45 mmol/g, after 3 consecutive reaction cycles. However, a gradual decline in activity was observed over successive cycles. By the 10th cycle, the hydrogen yield decreased to approximately 30 % of its initial value. This reduction was attributed to the progressive accumulation of pyrolysis byproducts, such as coke and unconverted carbonaceous residues, on the catalyst surface [71,72]. These deposits likely blocked active sites, hindered reactant access, and reduced catalytic efficiency. As cycling progressed, the buildup of such deactivating species intensified, further compromising hydrogen evolution and overall catalyst performance [16,73]. To verify this, we conducted HAADF-STEM analysis of the spent catalysts. The results clearly show that carbonaceous deposits encapsulate the metal nanoparticles after reaction (Supplementary Data, Figure S9). The originally well-defined lattice fringes of Fe/Ni were coated with coke, and the spatial overlap between carbon and metal domains strongly indicates that the active sites were blocked by deposited carbon species.

Catalyst regeneration was subsequently performed. Following five consecutive use cycles, the spent catalysts were treated according to a reported procedure [74]. Figure S10 compares the H_2 generation performance of the fresh, spent, and regenerated catalysts, and a significant catalytic performance increase was observed after regeneration. For example, the H_2 yield was improved from 25.36 mmol/g of the spent catalyst to 42.72 mmol/g of the regenerated catalyst, recovered 80 % of the fresh catalyst. While these results are promising, further work will be carried out to better design a regeneration procedure to address this critical issue.

3.3. Characterization of carbon materials

Carbon was the predominant solid product obtained from the microwave-assisted reaction. SEM and TEM analyses confirmed the presence of multi-walled carbon nanotubes (MWCNTs) within the carbonaceous materials (Fig. 6 and Supplementary data Figure S11). As the reaction temperature increased from 300 °C to 800 °C, the amount of granular material decreased, while MWCNTs became more abundant and increasingly dominated the SEM field of view. Typically, the MWCNTs exhibited inner diameters ranging from 2.1 to 5.3 nm and outer diameters from 5.7 to 10.4 nm (Fig. 6). Most of the metal catalyst particles were encapsulated within the nanotube walls, predominantly located at the midpoint or tip, indicating that a tip-growth mechanism as the dominant mode of CNT formation [68]. Overall, the carbon structures were primarily composed of entangled MWCNT bundles interspersed with dispersed particles. Such morphology facilitates the formation of continuous conductive pathways for mobile charge carriers, making these carbon nanostructures particularly attractive for applications in EMI shielding [75,76].

Raman spectroscopy was conducted to evaluate the structural order and defect characteristics of the carbonaceous products. The spectrum displayed two prominent peaks at ~1350 cm^{-1} (D band) and ~1580 cm^{-1} (G band), associated with the A_1g out-of-plane breathing mode of disordered carbon structures and the E_2g in-plane stretching mode of graphitic sp^2 carbon domains, respectively. The D band arises from lattice imperfections in the hexagonal carbon network, originating from either tetrahedral (sp^3) defects or distorted trigonal (sp^2) arrangements, while the G band corresponds to the crystalline graphitic ordering of sp^2 hybridized carbon atom [77,78].The measured I_D/I_G ratio of approximately 0.84 suggests the degree of graphitization is

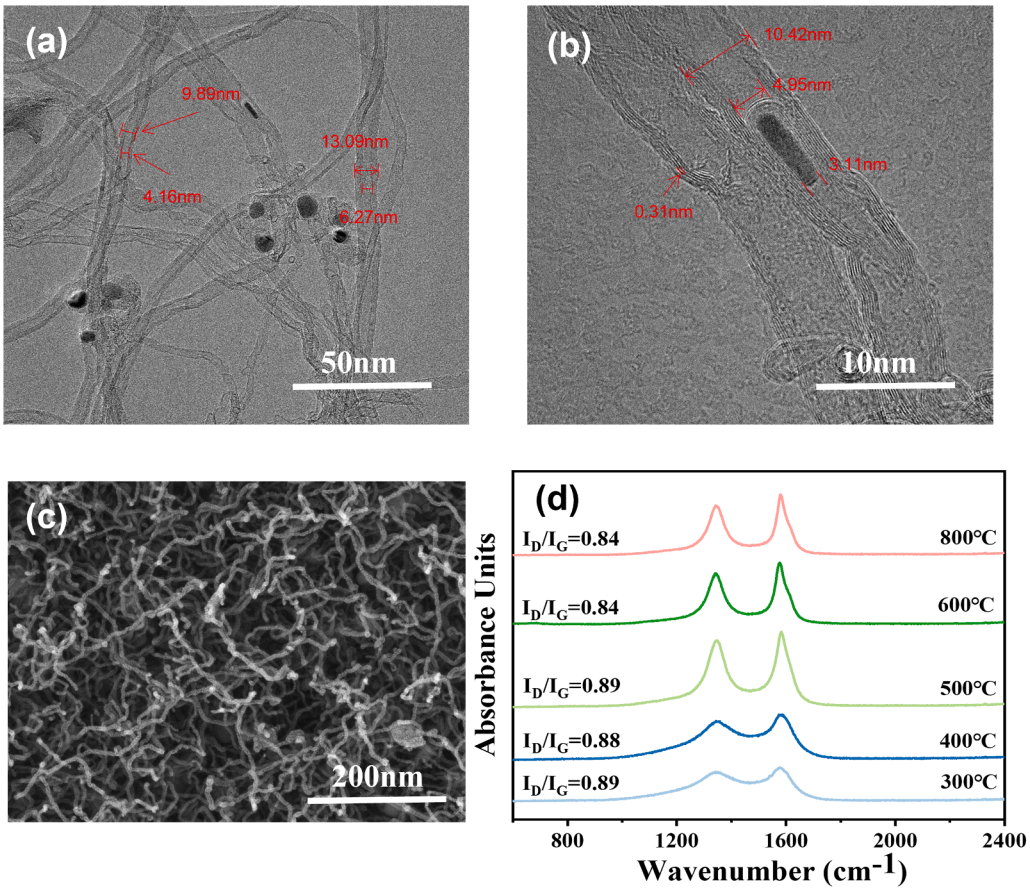

Fig. 6. Representative TEM (a-b) and SEM (c) images of the carbon materials from LDPE upcycling catalyzed with Fe/Ni-0.3 %Pt at 600 °C; (d) Raman spectra of the carbon materials generated from LDPE upcycling catalyzed by Fe/Ni-0.3 %Pt at different temperatures.

relatively high. The carbon material exhibits superior properties compared to those obtained through pyrolysis using a conventional furnace (Supplementary data Figure S12). The I_D /I_G ratio of the representative carbon materials obtained in this study catalyzed by Fe/Ni-0.3 %Pt with microwave treatment was lower than that of a widely used commercial MWCNTs (NC7600 manufactured by Nanocyl, Belgium) (0.84 vs. 1.2) (Supplementary data Figure S12).

3.4. Proposed reaction mechanism

Oxygen vacancies play a crucial role in plastic pyrolysis by serving as defect sites, facilitating C-H bond activation and cleavage [79–81]. Peng et al. [79]and Zhu et al. [80] both proposed that oxygen vacancies are conducive to the generation and transfer of reactive oxygen species. The transfer causes these reactive oxygen species to appear in a new form (O_{ads}), and the continuously provided electrons in this process trigger the cleavage of the C-H bond. Notably, the incorporation of very small amounts of Pt was found to significantly increase the concentration of oxygen vacancies. XPS analysis of the O 1 s spectra revealed that Pt addition (0.3 %) resulted in a nearly 23 % increase in the proportion of oxygen-deficient species, suggesting improved surface reactivity of the catalyst (Fig. 7). Meanwhile, it can be inferred that the increase in O_{ads} is due to the adsorption of surface oxygen vacancies and the activation of active oxygen species to generate adsorbed oxygen. This mechanism promotes the redox performance of the catalyst [82].

Li et al. [10] investigated microwave-assisted cracking of polyolefins and proposed that oxygen vacancies can be replenished by oxygen originating from water molecules, with hydrogen playing a pivotal role in the redox-mediated regeneration of surface oxygen species. Building upon this insight, we propose an alternative pathway, after C-C random breakage into short chains, they absorb on the surface of Pt. In situ catalysis by Pt activates the C-H bond, generating surface intermediates and Pt-H species [83]. Subsequently, these mobile hydrogen species migrate to the adjacent catalytic interface. They react with the active oxygen species on the metal oxide surface, generating alkyl radicals (R·) and H_2O. The direct involvement of Pt and reactive oxygen species lowers the activation barrier for C–H bond cleavage [84]. During this process, redox-active metal centers, such as Fe ($Fe^{3+} \leftrightarrow Fe^{2+} \leftrightarrow Fe^0$) and Ni ($Ni^{3+} \leftrightarrow Ni^{2+} \leftrightarrow Ni^0$), promote the rapid migration and replenishment of lattice oxygen through a reversible redox cycle, enabling continuous participation of O^{2-} in hydrocarbon activation [85]. Once H_2O molecules are polarized under microwave irradiation, the dissociation energy of the O–H bond is further reduced, thereby enhancing their interaction with adjacent oxygen vacancies. This interaction leads to the heterolytic dissociation of H_2O at Fe/Ni catalytic sites, generating H^+ and OH^- species via electron transfer mechanisms [10]. The resulting protons (H^+) combine with electrons to eventually form H_2, whereas the OH^- species will occupy the oxygen vacancy site, thereby restoring the lattice structure [86].

It is worth noting that strong acid sites play a critical role in polymer cracking reactions, as polymer activation typically initiates via adsorption and protonation at these sites, subsequently inducing C–C bond cleavage. Acid sites on catalysts are typically classified based on their strength and corresponding activation temperature: weak ($T < 250°C$), medium ($250°C < T < 350°C$), and strong ($T > 350°C$) acid sites [10]. Strong acid sites facilitate cracking and hydrogen transfer reactions through the formation of carbocation intermediates, which significantly enhances the selectivity toward gaseous and short-chain hydrocarbons. This results in higher yields of low-molecular-weight olefins and hydrogen-rich gaseous products [10]. Elevated reaction temperatures

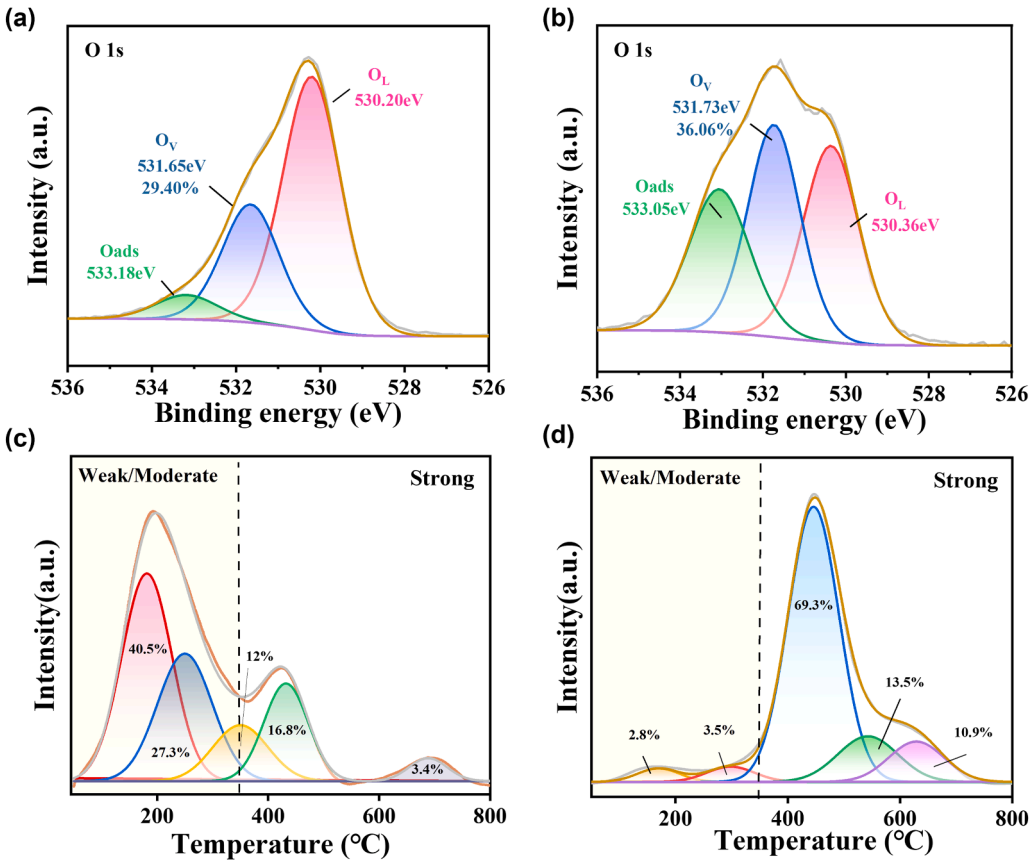

Fig. 7. Surface oxygen species and acid site distribution of Fe/Ni-based catalysts. High-resolution O 1 s XPS spectra showing the relative proportions of surface oxygen species for (a) Fe/Ni and (b) Fe/Ni–0.3 %Pt catalysts. Deconvoluted peaks correspond to lattice oxygen (O_L), oxygen vacancies (O_V), and adsorbed oxygen species (O_{ads}). NH_3-TPD profiles illustrating the acid site strength distribution for (c) Fe/Ni and (d) Fe/Ni–0.3 %Pt catalysts. Peaks above 350 °C represent strong acid sites. The ratio of strong acid peak area to total desorption peak area reflects the proportion of strong acid sites in each sample.

generally intensify these acid-catalyzed processes, resulting in higher yields of low-molecular-weight products; however, excessively high temperatures may also induce secondary reactions such as aromatization, oligomerization, and polycondensation, which not only shift product selectivity toward heavy polyaromatics but also promote coke deposition on the catalyst surface [87,88].

The dispersed Fe/Ni system exhibits predominantly weak acid sites [10,88]. As shown in Fig. 7c, the Fe/Ni alloy catalyst prepared in the current work possessed only about 30 % strong acid sites, favoring milder cracking of high-molecular-weight hydrocarbons. These catalysts preferentially promote double-bond isomerization reactions rather than extensive cracking, resulting in longer-chain hydrocarbons and increased yields of liquid-phase products while minimizing the formation of small molecules or undesirable byproducts like coke [87]. Upon incorporation of very small amounts of Pt, the overall acidic sites decreased slightly (Supplementary data Table 1). However, the proportion of strong acid sites increased substantially to approximately 94 % after Pt modification (Fig. 7d), resulting in a 3.3-fold increase in strong acidity (105.9 vs. 32.5 mmol/g). These sites enhanced polymer activation under microwave heating, where local electric fields and dielectric heating concentrated energy at acid centers. The resulting field-enhanced temperature enabled selective bond cleavage while suppressing random thermal cracking pathways [10]. This increase in strong acidity indicates that the Pt-modified Fe/Ni promoted intensive cracking and hydrogen transfer reactions, thereby improving selectivity toward light hydrocarbons and hydrogen.

Oxygen vacancies and strong acid sites on the catalyst surface are expected to exhibit a synergistic correlation. As mentioned earlier, oxygen vacancies facilitate the activation of electron-rich C-H bonds in hydrocarbon chains, enabling their homolytic cleavage via electron transfer and polarization mechanisms. Simultaneously, strong acid sites promote β-scission of C-C bonds, thereby accelerating the depolymerization of long polyethylene chains into low-molecular-weight products [87] [89]. In contrast, weak acid sites primarily catalyze double-bond isomerization rather than bond cleavage, favoring the formation of longer hydrocarbon chain and thereby increasing liquid product yield (Fig. 7 and Supplementary data Figure S4, Table S4). NH_3-TPD analysis revealed a substantial increase in both acid site density and strength upon Pt incorporation, particularly in the high-temperature desorption region (T > 350 °C), characteristic of strong acid sites. This enhancement is attributed to Pt-induced formation of oxygen vacancies within the metal oxide lattice, which generate additional coordinatively unsaturated metal centers. These defect sites not only serve as additional Lewis acid sites but also modulate the local electronic environment, thereby increasing the surface acidity and catalytic activity [10,90]. The significant improvement in hydrogen production is attributed to the fact that after Pt modification, the proportions of oxygen vacancies and strong acid sites increased significantly. The strong acid sites promoted the breaking of the C-C bond, while the oxygen vacancies facilitated the activation and cleavage of the C-H bond. The synergy between the two effects effectively converts long-chain hydrocarbons into hydrogen gas and carbon materials.

It should be noted that NH_3-TPD primarily provides information on the total acidity and does not differentiate between Brønsted and Lewis acid sites. While Brønsted acid sites are generally regarded as the main active sites for C–C activation, recent studies have shown that Lewis acids can also promote bond cleavage of C–C/C–H [91–93]. Further studies will be needed to distinguish the specific roles of Brønsted and

Lewis acid sites.

As confirmed by XRD analysis, $Fe_{0.18}Ni_{0.82}O_x$ and Fe_3O_4 were the predominant crystalline phases of the catalyst. Experimental results suggest that the oxygen vacancy concentration played a crucial role in the cleavage of C-H bonds. In order to evaluate the effect of Pt doping on oxygen vacancy formation, first-principles calculations were performed to determine the formation energy of oxygen vacancies on the (111) surface of Fe_3O_4 before and after Pt incorporation (Figures 8 and S9). As shown in Fig. 8, Pt doping significantly lowered the oxygen vacancy formation energy. For vacancy site Va at the first layer of the (111) surface of Fe_3O_4, the formation energy decreased from −0.77 eV (pristine) to −3.8 eV (Pt-doped). Similarly, the formation energy of V_b, another kind of oxygen vacancy, dropped from −0.79 eV to −5.2 eV, exhibiting an even greater reduction. The substantial reduction of formation energies indicates that Pt doping thermodynamically stabilized oxygen vacancies by modifying the electronic structure and facilitating charge redistribution.

We further investigated $Fe_{0.18}Ni_{0.82}O_x$, which is more catalytically relevant in our system (Figures 8 and S10). Pt doping decreased the formation energy of surface oxygen vacancies (V_o) from 1.53 eV to 0.28 eV, further confirming its role in promoting vacancy generation. These results demonstrate that Pt doping is an effective strategy for thermodynamically stabilizing oxygen vacancies on both Fe_3O_4 and $Fe_{0.18}Ni_{0.82}O_x$ surfaces, thereby enhancing catalytic activity through increased surface defect concentration.

To gain deeper insight into the dehydrogenation mechanism, an integrated microwave reactor–mass spectrometry (MW–GC-MS) system was employed to capture and identify intermediate species (Supplementary Data Table S2 and Table S3). Note that sampling posed a challenge because the reaction proceeds rapidly, and a delay in collecting products from the reaction tube can lead to further transformations. In addition, the resulting product mixture is highly complex. Nevertheless, several branched olefins were detected among the intermediates (Table S2), which are typical dehydrogenation products of iso-alkane intermediates. Furthermore, a substantial amount of iso-alkanes was identified in the final products (Table S3). These results collectively provide strong experimental support for a β-scission mechanism.

Given the complexity of byproducts generated during LDPE conversion, the analysis specifically focused on the dehydrogenation step leading to the formation of olefinic bonds. The abundant detection of 1-alkenes, isoalkanes and conjugated alkenes, together with their sequential appearance, suggests a dehydrogenation pathway initiated by terminal C–H bond dissociation to produce 1-alkenes, followed by isomerization into relatively stable conjugated olefins, and subsequent partial deep dehydrogenation. To elucidate the stepwise dehydrogenation process, density functional theory (DFT) calculations were performed using butane as a model compound. Butane was selected as the representative model molecule for our DFT calculations because: 1) during both thermal and catalytic cracking of polyethylene, butane is consistently identified as one of the major primary gaseous products [94], and it was also detected in our own product spectrum (approximately 28 % in the hydrocarbons, Supplementary Data Table S3); 2) its simple linear structure allows for a clear and computationally tractable mapping of the elementary C–H activation, dehydrogenation, and β-scission pathways, while avoiding the additional complexity associated with branched or long-chain intermediates; 3) butane has been widely employed in previous mechanistic and computational studies of long hydrocarbon activation [95,96]. Experimental results had confirmed $Fe_{0.18}Ni_{0.82}O_x$ as the primary active phase for alkane cracking and hydrogen evolution. We investigated the dehydrogenation pathway of butane on the (111) surface of $Fe_{0.18}Ni_{0.82}O_x$ by calculating the relative energy changes along the reaction coordinate, enabling construction of a complete potential energy profile (Fig. 9).

Initially, the butane molecule adsorbs onto the catalyst surface, forming a stable intermediate ($Fe_{0.18}Ni_{0.82}O_x$-$CH_3CH_2CH_2CH_3$*) with an adsorption energy of –0.37 eV. The first dehydrogenation step involves the breaking of C–H bonds at the terminal carbon and its adjacent carbon atom, leading to the formation of a surface-bound intermediate ($Fe_{0.18}Ni_{0.82}O_x$-$CH_2CHCH_2CH_3$*), accompanied by Ni–H bond formation on the catalyst surface. This transformation presents an energy barrier of 1.1 eV, representing the rate-determining step of the overall

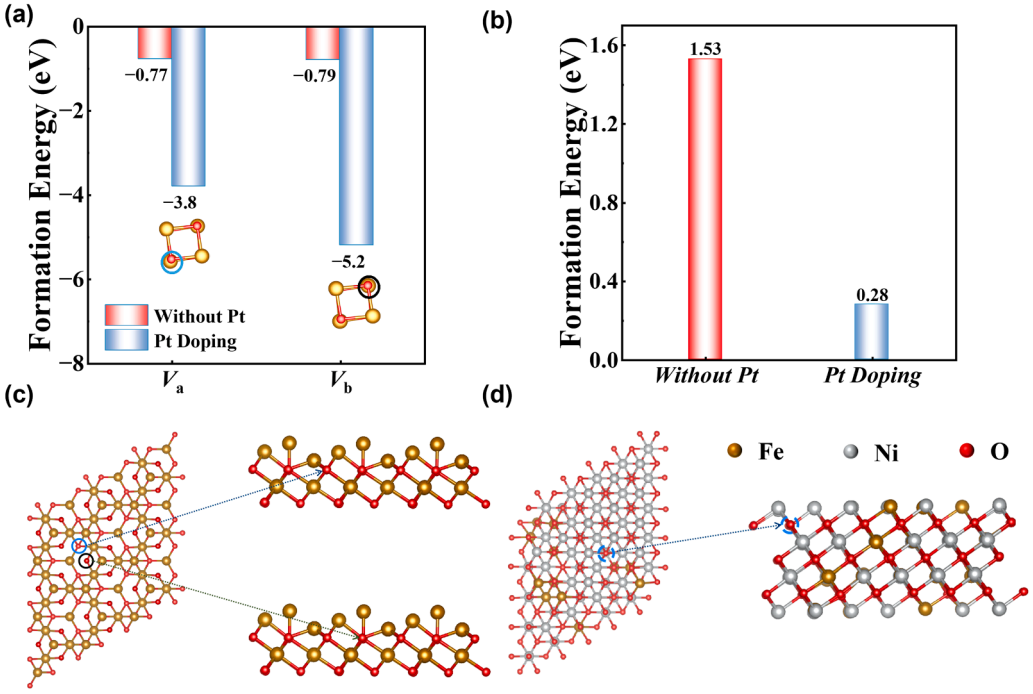

Fig. 8. Oxygen vacancy formation energy: (a) Two types of oxygen vacancy and their formation energies (eV) of the (111) surface. V_a and V_b represent the oxygen vacancies marked with blue and black circle at the first layer of (111) surface of Fe_3O_4. (b) The oxygen vacancy formation energies of the $Fe_{0.18}Ni_{0.82}O_x$. (c) Representation of two symmetrical oxygen vacancies of the (111) surface of Fe_3O_4; and (d) Oxygen vacancies of $Fe_{0.18}Ni_{0.82}O_x$.

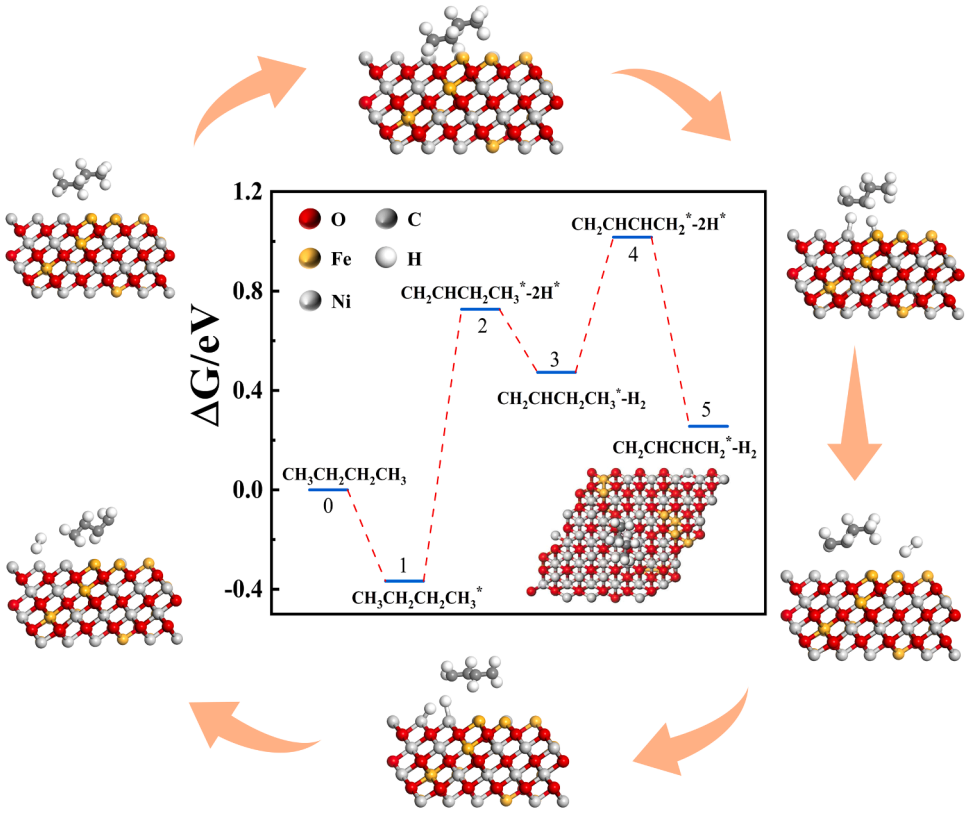

Fig. 9. The relative energy profile of the stepwise dehydrogenation of LDPE catalyzed by $Fe_{0.18}Ni_{0.82}O_x$ under microwave treatment as calculated by DFT. Grey, white, yellow, silver and red represent C, H, Fe, Ni, and O atoms respectively.

process. The resulting product corresponds to 1-butene. Subsequent dehydrogenation proceeds via cleavage of additional C–H bonds at the opposite terminal and its adjacent carbon atom, resulting in the formation of a second C═C bond and generation of 1,3-butadiene. Notably, the energy barrier for forming the second double bond is lower than that for the first, indicating that the conjugated diene structure provides additional thermodynamic stabilization and acts as a driving force for continued dehydrogenation.

These results suggest that $Fe_{0.18}Ni_{0.82}O_x$ not only effectively stabilizes key transition states but also promotes the stepwise removal of hydrogen atoms, ultimately favoring the formation of high-value conjugated olefins and H_2. This insight highlights the importance of designing catalysts that facilitate initial C–H bond activation and benefit from conjugation effects in later steps, thereby lowering energy barriers and improving hydrogen production efficiency.

3.5. Applicability to real-world polyolefins wastes and EMI shielding applications

The catalytic performance of Fe/Ni-Pt was further evaluated using post-consumer plastic wastes, including LDPE, LLDPE, HDPE, and PP, to assess its practical viability for processing real-world polyolefin waste streams under microwave-assisted conditions (Fig. 10). Hydrogen yields ranged from 47.7 to 53.1 mmol/g of plastic, with hydrogen selectivity values between 0.87 and 0.92, comparable to those obtained from the virgin LDPE (54.0 mmol/g and 0.90 selectivity). These results confirmed the feasibility of converting real-world polyolefin waste streams into high-value hydrogen and carbon materials under microwave-assisted conditions. Notably, all feedstocks exhibited consistently high hydrogen selectivity (>0.87). This suggests that under the high-energy microwave field, the reaction pathway favors dehydrogenation over the formation of complex hydrocarbons. It contrasts with conventional pyrolysis, where a broader spectrum of oxygenated compounds and hydrocarbon derivatives are typically produced [97,98].

It should be noted that H_2 yield from our post-consumer polyolefin wastes (LDPE*, HDPE*, PP*, and LLDPE*) are not significantly different, with a typical variation of 10 % (50.3, 53.1, 47.7, and 51.9 mmol g^{-1} plastic, respectively). The influence of polymer structure on hydrogen generation is a possible reason, though it has not yet been extensively explored. Previous studies reported that PP exhibits slightly lower C–C bond dissociation energies than PE because of the presence of tertiary carbons along its backbone [3]. The methyl substituent on each repeat unit introduces tertiary and secondary carbon centers that promote the formation of branched (iso-) intermediates during pyrolysis. These intermediates preferentially follow pathways leading to condensable liquid hydrocarbons rather than light gaseous species. In contrast, the linear backbone of PE decomposes more readily into linear olefins and light alkanes, which are easily dehydrogenated on metal sites to form H_2. Jie et al. also showed a slightly higher H_2 yield from HDPE as compared to PP (55.6 vs. 51.4 mmol g^{-1} plastic) under microwave-initiated catalytic deconstruction of plastic waste [11]. Liu et al. reported similar H_2 yields from linear polyolefin plastics (LLDPE, HDPE, and PP) with approximately 50 mmol g^{-1} plastic [23]. Therefore, consistent with these reports, the H_2 yield from PP in our study is slightly lower than that from PE, and the overall difference appears not very significant.

Benefiting from the impressive catalytic performance of Fe/Ni-0.3 % Pt, polyolefin waste was effectively converted into carbon-based materials suitable for EMI shielding applications. To evaluate the EMI shielding performance, the catalytic product obtained from the reaction at 600 °C were mixed with paraffin wax at designated mass ratios to fabricate composite specimens. As shown in Fig. 11, the SE_T increased substantially with higher filler content. Above 30 % loading, R is higher than A, indicating a reflection-dominated shielding mechanism. Notably, the SE_T reached an impressive 78 dB at a concentration of 40 wt% catalytic product, corresponding to a shielding efficiency

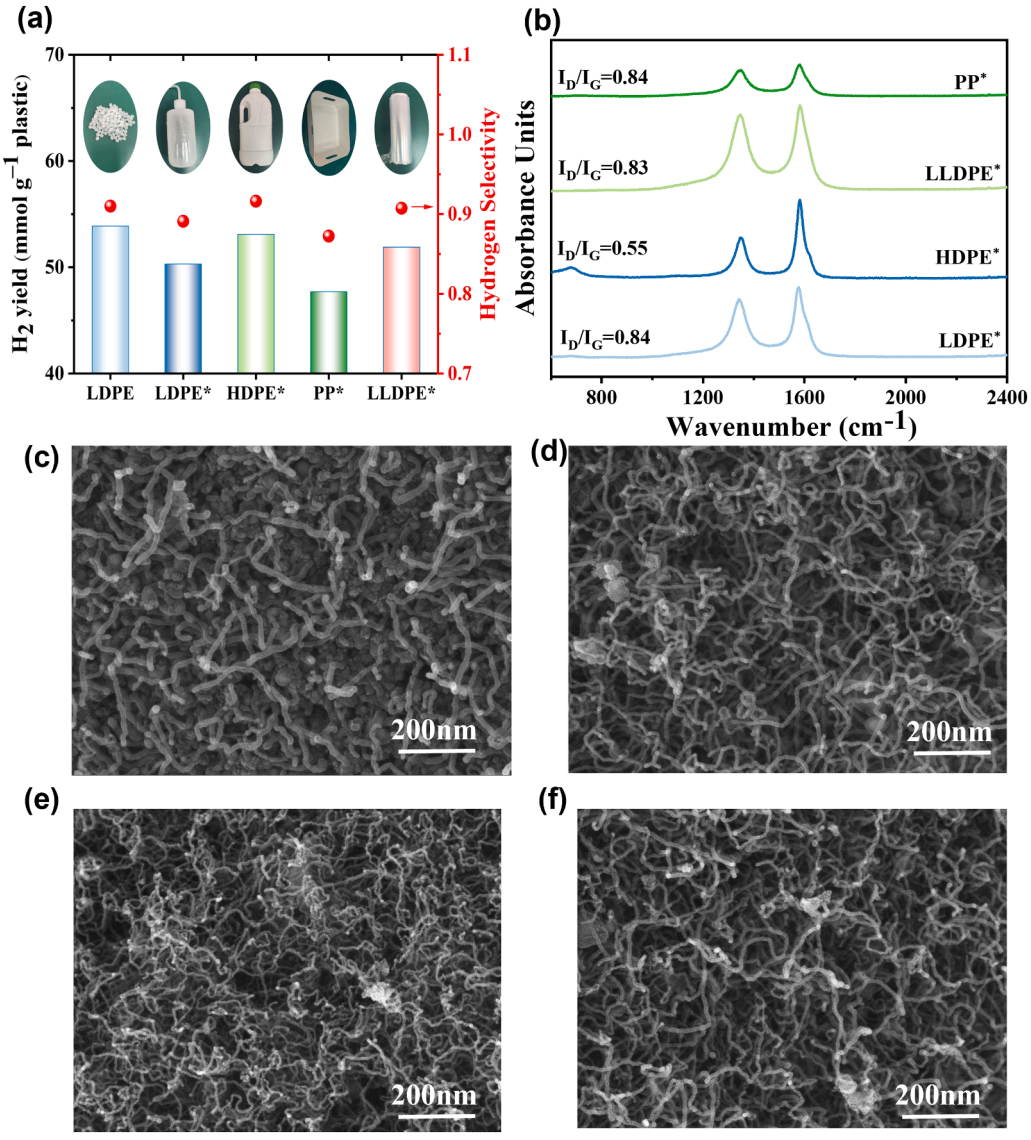

Fig. 10. (a) Hydrogen production and selectivity catalyzed by using LDPE,HDPE,LLDPE and PP in laboratory waste respectively at 600 ° C with Fe/Ni-0.3 %Pt (* indicates waste plastics); (b) The Raman values of the carbon materials generated after the reactions of the above-mentioned different laboratory wastes; (c-f) SEM images of carbon materials generated from PP*, LLDPE*, HDPE*, and LDPE*, respectively.

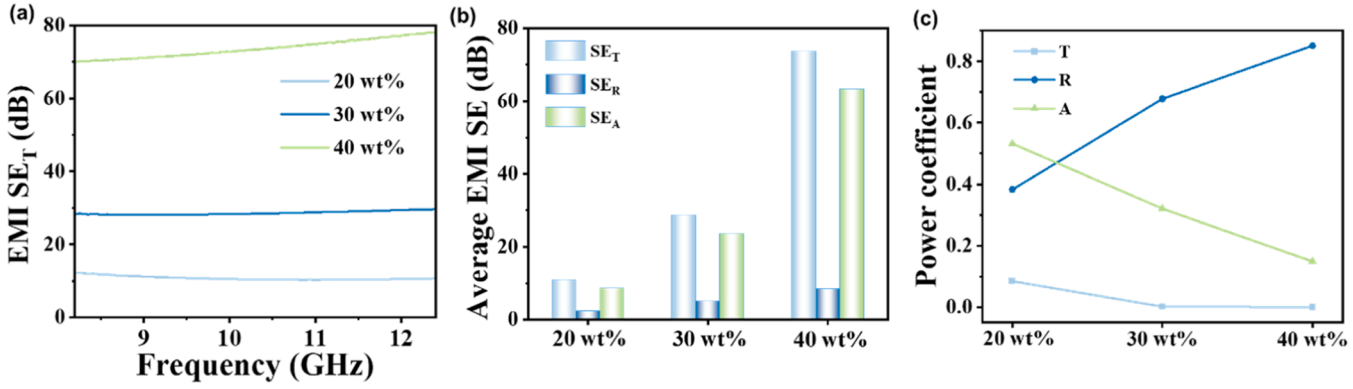

Fig. 11. (a) EMI SE in the range of 8.2–12.4 GHz; (b) Average values of EMI SE; (c) Average values of power coefficient for the composites containing 20 wt%, 30 wt % and 40 wt% solid products obtained from the microwave treatment of LDPE at 600 °C with Fe/Ni-0.3 %Pt.

exceeding 99.99999 %. These results highlight the strong potential of the upcycled carbon materials for use in high-performance EMI shielding applications.

4. Conclusion

In this study, a Fe/Ni-Pt bimetallic catalyst was developed for upcycling polyolefin wastes into H_2 and high-quality MWCNTs under microwave irradiation. Incorporation of trace Pt (e.g., 0.3 %) substantially reduced the oxygen vacancy formation energy and increased strong acid site density by 3.3-fold, as confirmed by experimental characterization and DFT calculations. These synergistic effects enhanced C–H and C–C bond activation, resulting in a high hydrogen yield of 53.9 mmol/g with 90 % selectivity from LDPE under optimal microwave conditions. Compared with thermal pyrolysis, the microwave-assisted approach achieved a 40 % reduction in energy consumption while maintaining a high plastic decomposition efficiency. Mechanistic studies revealed that the reaction proceeds via terminal C–H bond activation, conjugated olefin formation, and subsequent deep dehydrogenation. The resultant MWCNTs exhibited excellent EMI shielding performance, and the process proved effective for a range of real-world polyolefin wastes, underscoring its practical applicability. These findings highlight defect engineering and acidity modulation as a generalizable design strategy for next-generation microwave-assisted catalysts, advancing sustainable plastic waste-to-resource technologies.

CRediT authorship contribution statement

Yuhao Qiao: Writing – review & editing, Writing – original draft, Visualization, Methodology, Investigation, Formal analysis, Data curation, Conceptualization. **Xuanyan Chen:** Writing – original draft, Investigation, Formal analysis. **Zixuan Wang:** Writing – review & editing, Methodology, Formal analysis. **Weihao Xu:** Writing – review & editing, Visualization, Validation. **Zecheng Gan:** Writing – review & editing, Validation, Supervision. **Jun Wang:** Writing – review & editing, Writing – original draft, Validation, Supervision, Resources, Project administration, Methodology, Funding acquisition, Conceptualization.

Declaration of Competing Interest

The authors declare that they have no known competing financial interests or personal relationships that could have appeared to influence the work reported in this paper.

Acknowledgements

The authors express their gratitude for the financial support provided by the Guangzhou Municipal Science and Technology Bureau (2025A04J7060), the Department of Education of Guangdong Province (2024ZDZX3007), and the Guangdong Provincial Project (2023QN10C586). The authors also appreciate the support from the Green e Materials Laboratory (GeM), the Materials Characterization and Preparation Facility (MCPF), the Materials, Design and Manufacturing Facility (MDMF) and the Redbird Materials Preparation Workshop (RBM-Lab) at the Hong Kong University of Science and Technology (Guangzhou).

Appendix A. Supporting information

Supplementary data associated with this article can be found in the online version at doi:10.1016/j.apcatb.2025.126214.

Data availability

Data will be made available on request.

References

[1] A. Stubbins, K.L. Law, S.E. Muñoz, T.S. Bianchi, L.X. Zhu, Plastics in the Earth system, Science 373 (2021) 51–55.
[2] R. Geyer, J.R. Jambeck, K.L. Law, Production, use, and fate of all plastics ever made, Sci. Adv. 3 (2017) e1700782.
[3] J.K. Sun, J.H. Dong, L.J. Gao, Y.Q. Zhao, H. Moon, S.L. Scott, Catalytic Upcycling of Polyolefins, Chem. Rev. 124 (2024) 9457–9579.
[4] J. Zhao, B.N. Liu, L.Q. Xiong, W.C. Liu, D.D. Wang, W.J. Ma, L.T. Jiang, J.L. Yang, P. Wang, T.C. Xiao, S. Zhao, P.P. Edwards, J.W. Tang, Highly selective upcycling of plastic mixture waste by microwave-assisted catalysis over Zn/b-ZnO, Nat. Commun. 16 (2025) 1726.
[5] A. Bazargan, G. McKay, A review–synthesis of carbon nanotubes from plastic wastes, Chem. Eng. J. 195 (2012) 377–391.
[6] S.L. Wong, N. Ngadi, T.A.T. Abdullah, I.M. Inuwa, Current state and future prospects of plastic waste as source of fuel: A review, Renew. Sustain. Energy Rev. 50 (2015) 1167–1180.
[7] K.V. Popov, V.D. Knyazev, Initial stages of the pyrolysis of polyethylene, J. Phys. Chem. A 119 (2015) 11737–11760.
[8] A. Musa, E. Jaseer, S. Barman, N. Garcia, Review on catalytic depolymerization of polyolefin waste by hydrogenolysis: state-of-the-art and outlook, Energy Fuels 38 (2024) 1676–1691.
[9] Q. Hu, S. Qian, Y. Wang, J. Zhao, M. Jiang, M. Sun, H. Huang, T. Gan, J. Ma, J. Zhang, Polyethylene hydrogenolysis by dilute RuPt alloy to achieve H2-pressure-independent low methane selectivity, Nat. Commun. 15 (2024) 10573.
[10] J.L. Li, K.L. Chen, L. Lin, S.Y. Han, F.Z. Meng, E.D. Hu, W.K. Qin, Y.C. Gao, J. G. Jiang, Product Selection Toward High-Value Hydrogen and Bamboo-Shaped Carbon Nanotubes from Plastic Waste by Catalytic Microwave Processing, Environ. Sci. Technol. 58 (2024) 14675–14686.
[11] X.Y. Jie, W.S. Li, D. Slocombe, Y.G. Gao, I. Banerjee, S. Gonzalez-Cortes, B.Z. Yao, H. AlMegren, S. Alshihri, J. Dilworth, J. Thomas, T.C. Xiao, P. Edwards, Microwave-initiated catalytic deconstruction of plastic waste into hydrogen and high-value carbons, Nat. Catal. 3 (2020) 902–912.
[12] Q. Cao, H.C. Dai, J.H. He, C.L. Wang, C. Zhou, X.F. Cheng, J.M. Lu, Microwave-initiated MAX Ti3AlC2-catalyzed upcycling of polyolefin plastic wastes: selective conversion to hydrogen and carbon nanofibers for sodium-ion battery, Appl. Catal. B Environ. Energy 318 (2022) 121828.
[13] Z. Jiang, Y. Liang, F. Guo, Y. Wang, R. Li, A. Tang, Y. Tu, X. Zhang, J. Wang, S. Li, Microwave-assisted Pyrolysis-A new way for the sustainable recycling and upgrading of plastic and biomass: a review, ChemSusChem (2024) e202400129.
[14] W.T. Li, K.Z. Qian, Z.X. Yang, X.X. Ding, W.M. Tian, D.Z. Chen, Promotion effect of cobalt doping on microwave-initiated plastic deconstruction for hydrogen production over iron catalysts, Appl. Catal. B Environ. Energy 327 (2023) 122451.
[15] X. Bai, P.D. Muley, T. Musho, V. Abdelsayed, B. Robinson, A. Caiola, D. Shekhawat, C. Jiang, J. Hu, A combined experimental and modeling study of Microwave-assisted methane dehydroaromatization process, Chem. Eng. J. 433 (2022) 134445.
[16] Y.X. Wang, T. Biddle, C.L. Jiang, T. Luong, R.J. Chen, S. Brown, X.Y. Jie, J.L. Hu, Microwave-driven upcycling of single-use plastics using zeolite catalyst, Chem. Eng. J. 465 (2023) 142918.
[17] C. Jiang, A. Araia, S. Balyan, B. Robinson, S. Brown, A. Caiola, J. Hu, J. Dou, L. M. Neal, F. Li, Kinetic study of Ni-M/CNT catalyst in methane decomposition under microwave irradiation, Appl. Catal. B Environ. 340 (2024) 123255.
[18] C. Mevawala, X. Bai, D. Bhattacharyya, J. Hu, Dynamic data reconciliation, parameter estimation, and multi-scale, multi-physics modeling of the microwave-assisted methane dehydroaromatization process, Chem. Eng. Sci. 239 (2021) 116624.
[19] J.C. Acomb, C.F. Wu, P.T. Williams, The use of different metal catalysts for the simultaneous production of carbon nanotubes and hydrogen from pyrolysis of plastic feedstocks, Appl. Catal. B Environ. 180 (2016) 497–510.
[20] J. Luo, G.J. Gong, R. Ma, S.C. Sun, C.W. Cui, H. Cui, J.M. Sun, N. Ma, Study on high-value products of waste plastics from microwave catalytic pyrolysis: Construction and performance evaluation of advanced microwave absorption-catalytic bifunctional catalysts, Fuel 346 (2023) 128296.
[21] J.C. Acomb, C.F. Wu, P.T. Williams, Effect of growth temperature and feedstock: catalyst ratio on the production of carbon nanotubes and hydrogen from the pyrolysis of waste plastics, J. Anal. Appl. Pyrolysis 113 (2015) 231–238.
[22] J. Wang, Y.H. Pan, J.X. Song, Q.X. Huang, A high-quality hydrogen production strategy from waste plastics through microwave-assisted reactions with heterogeneous bimetallic iron/nickel/cerium catalysts, J. Anal. Appl. Pyrolysis 166 (2022) 105612.
[23] Q. Liu, D. Jiang, H. Zhou, X. Yuan, C. Wu, C. Hu, R. Luque, S. Wang, S. Chu, R. Xiao, Pyrolysis–catalysis upcycling of waste plastic using a multilayer stainless-steel catalyst toward a circular economy, in: Proceedings of the National Academy of Sciences, 120, 2023.
[24] J. Zhao, J.Y. Gao, D.D. Wang, Y. Chen, L. Zhang, W.J. Ma, S. Zhao, Microwave-intensified catalytic upcycling of plastic waste into hydrogen and carbon nanotubes over self-dispersing bimetallic catalysts, Chem. Eng. J. 483 (2024).
[25] X. Liu, Y. Zhang, M.A. Nahil, P.T. Williams, C. Wu, Development of Ni-and Fe-based catalysts with different metal particle sizes for the production of carbon nanotubes and hydrogen from thermo-chemical conversion of waste plastics, J. Anal. Appl. Pyrolysis 125 (2017) 32–39.
[26] D. Yao, C.H. Wang, Pyrolysis and in-line catalytic decomposition of polypropylene to carbon nanomaterials and hydrogen over Fe- and Ni-based catalysts, Appl. Energy 265 (2020) 114819.

[27] D.D. Yao, Y.S. Zhang, P.T. Williams, H.P. Yang, H.P. Chen, Co-production of hydrogen and carbon nanotubes from real-world waste plastics: Influence of catalyst composition and operational parameters, Appl. Catal. B Environ. 221 (2018) 584–597.
[28] B. Zhang, Y.N. Li, S. Lu, Y. Hu, Y. Li, S. Wang, J. Liu, T. Tang, S. Li, Co-, Ni-, and Cu-Doped Fe-based catalysts for the microwave-assisted catalytic pyrolysis of polyethylene, ChemSusChem 17 (2024).
[29] L.S. Yao, B.K. Yi, X.Q. Zhao, W.L. Wang, Y.P. Mao, J. Sun, Z.L. Song, Microwave-assisted decomposition of waste plastic over Fe/FeAlO to produce hydrogen and carbon nanotubes, J. Anal. Appl. Pyrolysis 165 (2022) 105577.
[30] K.A. Shah, B.A. Tali, Synthesis of carbon nanotubes by catalytic chemical vapour deposition: a review on carbon sources, catalysts and substrates, Mater. Sci. Semicond. Process. 41 (2016) 67–82.
[31] E. Tezel, H.E. Figen, S.Z. Baykara, Hydrogen production by methane decomposition using bimetallic Ni–Fe catalysts, Int. J. Hydrog. Energy 44 (2019) 9930–9940.
[32] C. Zhang, S. Qin, H. Gao, P. Jin, High hydrogen evolution activities of dual-metal atoms incorporated N-doped graphenes achieved by coordination regulation, J. Mater. Inform. (2024).
[33] M. Pudukudy, Z. Yaakob, Z.S. Akmal, Direct decomposition of methane over Pd promoted Ni/SBA-15 catalysts, Appl. Surf. Sci. 353 (2015) 127–136.
[34] H. Ogihara, S. Takenaka, I. Yamanaka, E. Tanabe, A. Genseki, K. Otsuka, Formation of highly concentrated hydrogen through methane decomposition over Pd-based alloy catalysts, J. Catal. 238 (2006) 353–360.
[35] M. Pudukudy, Z. Yaakob, Q. Jia, M.S. Takriff, Catalytic decomposition of undiluted methane into hydrogen and carbon nanotubes over Pt promoted Ni/CeO 2 catalysts, N. J. Chem. 42 (2018) 14843–14856.
[36] S. Takenaka, Y. Shigeta, E. Tanabe, K. Otsuka, Methane decomposition into hydrogen and carbon nanofibers over supported Pd− Ni catalysts, J. Phys. Chem. B 108 (2004) 7656–7664.
[37] E. Odier, Y. Schuurman, C. Mirodatos, Non-stationary catalytic cracking of methane over ceria-based catalysts: Mechanistic approach and catalyst optimization, Catal. Today 127 (2007) 230–237.
[38] Z.A. Xie, Z. Li, P. Tang, Y.Y. Song, Z. Zhao, L.A. Kong, X.Q. Fan, X. Xiao, The effect of oxygen vacancies on the coordinatively unsaturated Al-O acid-base pairs for propane dehydrogenation, J. Catal. 397 (2021) 172–182.
[39] P.E. Blöchl, Projector augmented-wave method, Phys. Rev. B 50 (24) (1994) 17953.
[40] G. Kresse, J. Furthmuller, Efficiency of ab-initio total energy calculations for metals and semiconductors using a plane-wave basis set, Comput. Mater. Sci. 6 (1996) 15–50.
[41] A.I. Liechtenstein, V.I. Anisimov, J. Zaanen, Density-Functional Theory and Strong-Interactions - Orbital Ordering in Mott-Hubbard Insulators, Phys. Rev. B 52 (1995) R5467–R5470.
[42] S.L. Dudarev, D.N. Manh, A.P. Sutton, Effect of Mott-Hubbard correlations on the electronic structure and structural stability of uranium dioxide, Philos. Mag. BPhys. Condens. Matter Stat. Mech. Electron. Opt. Magn. Prop. 75 (1997) 613–628.
[43] H.J. Monkhorst, J.D. Pack, Special points for Brillouin-zone integrations, Phys. Rev. B 13 (1976) 5188.
[44] X. Zhang, J.X. Shen, M.E. Turiansky, C.G. Van de Walle, Minimizing hydrogen vacancies to enable highly efficient hybrid perovskites, Nat. Mater. 20 (2021) 971.
[45] L. Ning, M. Zhang, S. Liao, Y. Zhang, D. Jia, Y. Yan, W. Gu, X. Liu, Differentiation of Pt− Fe and Pt− Ni3 Surface Catalytic Mechanisms towards Contrasting Products in Chemoselective Hydrogenation of α, β-Unsaturated Aldehydes, ChemCatChem 13 (2021) 704–711.
[46] T. Yamashita, P. Hayes, Analysis of XPS spectra of Fe and Fe ions in oxide materials, Appl. Surf. Sci. 254 (2008) 2441–2449.
[47] C. Wang, W. Zhang, J. Wang, P. Xia, X. Duan, Q. He, I. Sirés, Z. Ye, Accelerating Fe (III)/Fe (II) redox cycling in heterogeneous electro-Fenton process via S/Cu-mediated electron donor-shuttle regime, Appl. Catal. B Environ. 342 (2024) 123457.
[48] E.L. Ratcliff, J. Meyer, K.X. Steirer, A. Garcia, J.J. Berry, D.S. Ginley, D.C. Olson, A. Kahn, N.R. Armstrong, Evidence for near-surface NiOOH species in solution-processed NiO x selective interlayer materials: impact on energetics and the performance of polymer bulk heterojunction photovoltaics, Chem. Mater. 23 (2011) 4988–5000.
[49] T. Pan, S.D. Ge, M.N. Yu, Y.N. Ju, R. Zhang, P. Wu, K.Y. Zhou, Z.J. Wu, Synthesis and consequence of Zn modified ZSM-5 zeolite supported Ni catalyst for catalytic aromatization of olefin/paraffin, Fuel 311 (2022) 122629.
[50] K. Fominykh, J.M. Feckl, J. Sicklinger, M. Döblinger, S. Böcklein, J. Ziegler, L. Peter, J. Rathousky, E.W. Scheidt, T. Bein, Ultrasmall dispersible crystalline nickel oxide nanoparticles as high-performance catalysts for electrochemical water splitting, Adv. Funct. Mater. 24 (2014) 3123–3129.
[51] Q.L. Wu, Z. Li, X.H. Zhang, C.Y. Xu, M.J. Ni, K.F. Cen, Y.W. Zhang, Oxygen-vacancy-anchoring NiO loading towards efficient hydrogen evolution via photo-thermal coupling reaction, J. Energy Chem. 61 (2021) 77–87.
[52] C. Chen, J.B. Xi, E.Z. Zhou, L. Peng, Z.C. Chen, C. Gao, Porous graphene microflowers for high-performance microwave absorption, Nano Micro Lett. 10 (2018) 1–11.
[53] L.E. Gómez, B.M. Sollier, A.M. Lacoste, E.E. Miró, A.V. Boix, Hydrogen purification for fuel cells through CO preferential oxidation using PtCu/AlO structured catalysts, J. Environ. Chem. Eng. 7 (2019) 103376.
[54] S. Yang, D.Y. Chung, Y.J. Tak, J. Kim, H. Han, J.S. Yu, A. Soon, Y.E. Sung, H. Lee, Electronic structure modification of platinum on titanium nitride resulting in enhanced catalytic activity and durability for oxygen reduction and formic acid oxidation, Appl. Catal. B Environ. 174 (2015) 35–42.
[55] J. Cored, M.E. Wang, N. Akter, Z. Darbari, Y.X. Xu, B. Karagoz, I. Waluyo, A. Hunt, D. Stacchiola, A.R. Head, P. Concepcion, D.Y. Lu, J.A. Boscoboinik, Water Formation Reaction under Interfacial Confinement: AlSiO on O-Ru(0001), Nanomaterials 12 (2022) 183.
[56] C.M. Xu, P.X. Qiu, H. Chen, F. Jiang, Platinum modified indium oxide nanorods with enhanced photocatalytic activity on degradation of perfluorooctanoic acid (PFOA), J. Taiwan Inst. Chem. Eng. 80 (2017) 761–768.
[57] D.D. Yao, H. Li, Y.J. Dai, C.H. Wang, Impact of temperature on the activity of Fe-Ni catalysts for pyrolysis and decomposition processing of plastic waste, Chem. Eng. J. 408 (2021) 127268.
[58] S. Prabu, K.-Y. Chiang, Highly active Ni–Mg–Al catalyst effect on carbon nanotube production from waste biodegradable plastic catalytic pyrolysis, Environ. Technol. Innov. 28 (2022) 102845.
[59] L. Zhou, L.R. Enakonda, M. Harb, Y. Saih, A. Aguilar-Tapia, S. Ould-Chikh, J. L. Hazemann, J. Li, N. Wei, D. Gary, P. Del-Gallo, J.M. Basset, Fe catalysts for methane decomposition to produce hydrogen and carbon nano materials, Appl. Catal. B Environ. 208 (2017) 44–59.
[60] B. Luo, D.X. Kong, S.X. Wang, R. Shan, H.R. Yuan, Y. Chen, Hydrogen-rich gas by catalytic pyrolysis of polyethylene via mono and bimetallic Fe/Ni catalysts, Int. J. Hydrog. Energy 120 (2025) 181–188.
[61] B. Kunwar, H.N. Cheng, S.R. Chandrashekaran, B.K. Sharma, Plastics to fuel: a review, Renew. Sustain. Energy Rev. 54 (2016) 421–428.
[62] J.L. Wang, S.Z. Wang, Activation of persulfate (PS) and peroxymonosulfate (PMS) and application for the degradation of emerging contaminants, Chem. Eng. J. 334 (2018) 1502–1517.
[63] X. Tong, S.C. Ma, Y. Qi, J.Q. Li, T.J. Yao, J. Wu, Synthesis of FeCo alloy encapsulated nitrogen-doped graphitized carbon: High catalytic activation and low metal ion leaching in microwave assisted Fenton reaction, J. Taiwan Inst. Chem. Eng. 108 (2020) 64–70.
[64] C. Xu, P. Liu, Z. Wu, H. Zhang, R. Zhang, C. Zhang, L. Wang, L. Wang, B. Yang, Z. Yang, Customizing heterointerfaces in multilevel hollow architecture constructed by magnetic spindle arrays using the polymerizing-etching strategy for boosting microwave absorption, Adv. Sci. 9 (2022) 2200804.
[65] S. Głowniak, B. Szczęśniak, J. Choma, M. Jaroniec, Advances in microwave synthesis of nanoporous materials, Adv. Mater. 33 (2021) 2103477.
[66] B.A. Mohamed, N. Ellis, C.S. Kim, X.T. Bi, Microwave-assisted catalytic biomass pyrolysis: effects of catalyst mixtures, Appl. Catal. B Environ. 253 (2019) 226–234.
[67] A.A. Arpia, W.H. Chen, S.S. Lam, P. Rousset, M.D.G. de Luna, Sustainable biofuel and bioenergy production from biomass waste residues using microwave-assisted heating: a comprehensive review, Chem. Eng. J. 403 (2021) 126233.
[68] F. Vatankhah, A.C. García, J. Chaouki, Hydrogen and carbon nanotube production from microwave-assisted catalytic decomposition of plastic waste, Chem. Eng. J. 503 (2025) 158189.
[69] K. Ding, S.S. Liu, Y. Huang, S.Y. Liu, N. Zhou, P. Peng, Y.P. Wang, P. Chen, R. Ruan, Catalytic microwave-assisted pyrolysis of plastic waste over NiO and HY for gasoline-range hydrocarbons production, Energy Convers. Manag. 196 (2019) 1316–1325.
[70] R.R. Mishra, P.H. Rana, P.A. Parikh, Microwave-assisted pyrolysis of low-density polyethylene (LDPE) to value-added products over HY, HZSM-5 and Hβ catalyst, Mater. Today Commun. 41 (2024) 110829.
[71] C.H. Bartholomew, Mechanisms of catalyst deactivation, Appl. Catal. A Gen. 212 (2001) 17–60.
[72] E.T. Vogt, D. Fu, B.M. Weckhuysen, Carbon deposit analysis in catalyst deactivation, regeneration, and rejuvenation, Angew. Chem. Int. Ed. 62 (2023) e202300319.
[73] N. Zhou, L.L. Dai, Y.C. Lv, H. Li, W.Y. Deng, F.Q. Guo, P. Chen, H.W. Lei, R. G. Ruan, Catalytic pyrolysis of plastic wastes in a continuous microwave assisted pyrolysis system for fuel production, Chem. Eng. J. 418 (2021) 129412.
[74] H. Pan, D. Xu, C. He, C. Shen, In situ regeneration and deactivation of Co-Zn/H-Beta catalysts in catalytic reduction of NOx with propane, Catalysts 9 (2018) 23.
[75] Z.P. Wu, M.M. Li, Y.Y. Hu, Y.S. Li, Z.X. Wang, Y.H. Yin, Y.S. Chen, X.A. Zhou, Electromagnetic interference shielding of carbon nanotube macrofilms, Scr. Mater. 64 (2011) 809–812.
[76] D.D. Yao, C.F. Wu, H.P. Yang, Y.S. Zhang, M.A. Nahil, Y.Q. Chen, P.T. Williams, H. P. Chen, Co-production of hydrogen and carbon nanotubes from catalytic pyrolysis of waste plastics on Ni-Fe bimetallic catalyst, Energy Convers. Manag. 148 (2017) 692–700.
[77] H.N. Li, B. Yang, J.Q. Lu, X.K. Guo, B. Yu, Y. Xiong, N. Huang, L.S. Liu, G. Xu, X. Jiang, Tailoring the sp2/sp3 carbon composition for surface enhancement in Raman scattering, Appl. Surf. Sci. 599 (2022) 153966.
[78] X. Rao, J. Yang, Z. Chen, Y. Yuan, Q. Chen, X. Feng, L. Qin, Y. Zhang, Tuning C–C sp2/sp3 ratio of DLC films in FCVA system for biomedical application, Bioact. Mater. 5 (2020) 192–200.
[79] H.G. Peng, T. Dong, S.Y. Yang, H. Chen, Z.Z. Yang, W.M. Liu, C. He, P. Wu, J. S. Tian, Y. Peng, X.F. Chu, D.S. Wu, T.C. An, Y. Wang, S. Dai, Intra-crystalline mesoporous zeolite encapsulation-derived thermally robust metal nanocatalyst in deep oxidation of light alkanes, Nat. Commun. 13 (2022) 295.
[80] C.L. Zhu, S.S. Hou, X.L. Hu, J.H. Lu, F.L. Chen, K. Xie, Electrochemical conversion of methane to ethylene in a solid oxide electrolyzer, Nat. Commun. 10 (2019) 1173.
[81] S. Liu, H. Wang, S. Wang, Y. Dai, B. Liu, Y. Liu, F. Dang, K.J. Smith, X. Nie, S. Hou, Engineering morphology and Ni substitution of Ni x Co3–x O4 spinel oxides to promote catalytic combustion of ethane: elucidating the influence of oxygen defects, ACS Catal. 13 (2023) 4683–4699.

[82] M. Yang, G.L. Shen, Q. Wang, K. Deng, M. Liu, Y.F. Chen, Y. Gong, Z. Wang, Roles of Oxygen Vacancies of CeO and Mn-Doped CeO with the Same Morphology in Benzene Catalytic Oxidation, Molecules 26 (2021) 6363.
[83] J.A. Labinger, Platinum-catalyzed C–H functionalization, Chem. Rev. 117 (2017) 8483–8496.
[84] D. Tian, K. Li, Y. Wei, X. Zhu, C. Zeng, X. Cheng, Y. Zheng, H. Wang, DFT insights into oxygen vacancy formation and CH 4 activation over CeO 2 surfaces modified by transition metals (Fe, Co and Ni), Phys. Chem. Chem. Phys. 20 (2018) 11912–11929.
[85] M.D. Farahani, M. Wolf, T.P.O. Mkhwanazi, M. Claeys, H.B. Friedrich, Operando experimental evidence on the central role of oxygen vacancies during methane combustion, J. Catal. 390 (2020) 184–195.
[86] R. Ovcharenko, E. Voloshina, J. Sauer, Water adsorption and O-defect formation on Fe 2 O 3 (0001) surfaces, Phys. Chem. Chem. Phys. 18 (2016) 25560–25568.
[87] S. Papuga, M. Djurdjevic, A. Ciccioli, S. Vecchio Ciprioti, Catalytic pyrolysis of plastic waste and molecular symmetry effects: A review, Symmetry 15 (2022) 38.
[88] X. Wang, Q. Fang, J. Wang, K. Gui, H.R. Thomas, Effect of CaCO 3 on catalytic activity of Fe–Ce/Ti catalysts for NH 3-SCR reaction, RSC Adv. 10 (2020) 44876–44883.
[89] L. Chi, T. Wang, Q. Jiang, Design of Fe2Mo@ γ-GDY triatomic catalyst for electrocatalytic urea synthesis of N2 and CO: a theoretical study, J. Mater. Inform. 5 (2025).
[90] Z.X. Zhang, Y.H. Wang, J.M. Lu, C.F. Zhang, M. Wang, M.R. Li, X.B. Liu, F. Wang, Conversion of Isobutene and Formaldehyde to Diol using Praseodymium-Doped CeO Catalyst, Acs Catal. 6 (2016) 8248–8254.
[91] H. Gao, L. Hu, Y. Hu, X. Lv, Y.-B. Wu, G. Lu, Origins of Lewis acid acceleration in nickel-catalysed C–H, C–C and C–O bond cleavage, Catal. Sci. Technol. 11 (2021) 4417–4428.
[92] H. Ran, S. Zhang, W. Ni, Y. Jing, Precise activation of C–C bonds for recycling and upcycling of plastics, Chem. Sci. 15 (2024) 795–831.
[93] S. Kokuryo, K. Tamura, K. Miyake, Y. Uchida, A. Mizusawa, T. Kubo, N. Nishiyama, LDPE cracking over mono-and divalent metal-doped beta zeolites, Catal. Sci. Technol. 12 (2022) 4138–4144.
[94] P. Ylitervo, T. Richards, Gaseous products from primary reactions of fast plastic pyrolysis, J. Anal. Appl. Pyrolysis 158 (2021) 105248.
[95] M. Chu, X. Wang, X. Wang, P. Xu, L. Zhang, S. Li, K. Feng, J. Zhong, L. Wang, Y. Li, Layered double hydroxide derivatives for polyolefin upcycling, J. Am. Chem. Soc. 146 (2024) 10655–10665.
[96] C. Wu, L. Wang, Z. Xiao, G. Li, L. Wang, Understanding deep dehydrogenation and cracking of n-butane on Ni (111) by a DFT study, Phys. Chem. Chem. Phys. 22 (2020) 724–733.
[97] N. Mills, M. Jenkins, S. Kukureka, Plastics: microstructure and engineering applications, Butter Heinemann (2020).
[98] I. Ahmad, M.I. Khan, H. Khan, M. Ishaq, R. Tariq, K. Gul, W. Ahmad, Pyrolysis study of polypropylene and polyethylene into premium oil products, Int. J. Green. Energy 12 (2015) 663–671.